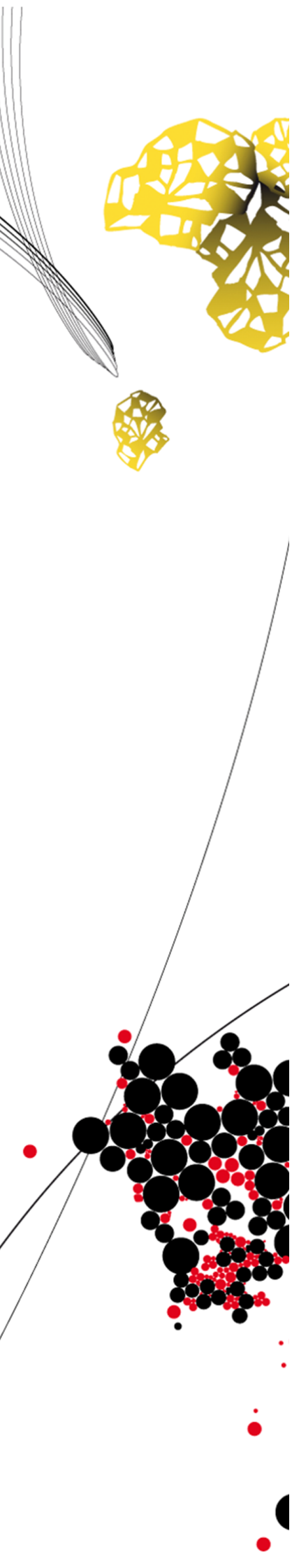

UNIVERSITY OF TWENTE.

Faculty of Electrical Engineering, Mathematics & Computer Science

Modeling, Characterizing and Evaluating the Wireless Link of the Patient Health Monitor.

Jan-Willem Nijhuis

M.Sc. Thesis
November 2021

Supervisors:
dr. ir. A.B.J. Kokkeler
dr. ir. Y. Miao
dr. ir. R.A.R. van der Zee
ir. M. Kleijnen (Philips)
ir. G. Doodemans (Philips)

Radio Systems Group
Faculty of Electrical Engineering,
Mathematics and Computer Science
University of Twente
P.O. Box 217
7500 AE Enschede
The Netherlands

Contents

Appendices

List of acronyms

LOS	line-of-sight
GTD	geometrical theory of diffraction
UTD	uniform theory of diffraction
SNR	signal-to-noise ratio
WPAN	wireless personal area network
UWB	ultra wideband
TE	transversal electric
TM	transversal magnetic
FEM	finite element method
MoM	method of moments
FDTD	finite-difference time-domain
RT	ray-tracing
RL	ray-launching
NLOS	non-line-of-sight
WBAN	wireless body area network
PDP	power delay profile
PO	physical optics
UWB	ultra wideband
BAN	body area network
ISI	intersymbol interference

BER	bit error rate
EDR	enhaced data rate
LE	low energy
DPSK	differential phase shift keying
LCR	level crossing rate
ADF	average duration of fades
BPM	burst position modulation
BPSK	binary phase-shift-keying
CIR	channel impulse response
RMSE	root-mean-square error
FEC	forward error correction
PER	packet error rate
cdf	cumulative distribution function

Chapter 1

Introduction

Wireless connected devices become more and more present in our daily lives. The lack of wires allows wireless devices to be placed anywhere within range. This is especially beneficial for devices carried by us, like mobile phones. In hospitals, vital signals of a patient's body are monitored as a precaution or to check the patient's recovery. Wireless monitors will allow patients to move freely within the hospital and ease their stay. However, the wireless connection needs to be reliable, as vital indicators are transmitted over it. It is therefore crucial to predict the wireless radio propagation accurately.

The radio propagation in an environment can be modeled by conducting many measurements in that particular environment. This is a very time consuming method though. Measurements in the end-use environment are not always possible as well. Radio propagation simulations provide a solution for this task, wherein the interaction between radio waves and a modeled environment can be simulated.

In the following section, the background and literature review on radio propagation simulation is given. Afterwards the motivation and goal for this research are given.

1.1 Background

In this section, the propagation mechanisms of radio waves are described. Thereafter, different simulation methods are described and a literature review is given.

Propagation Mechanisms

A radio channel consists of many radio waves propagating from a transmitter to a receiver. During the propagation, these radio waves are subject to multiple propagation mechanisms.

First of all, propagating radio waves lose power as they propagate. This is due to the fact that the radiated power spreads over an ever growing wavefront. In free space, this loss can be computed with equation 1.1,[1] where L_{FS} is the free space loss, λ is the wavelength and d is the propagation distance.

$$L_{\text{FS}} = \left(\frac{4\pi d}{\lambda}\right)^2 \tag{1.1}$$

When a radio wave impinges a surface of geometry, it will reflect back from that surface, and penetrate into it. The directions of outgoing radio waves depends on the reflection and transmission angles (figure 1.1). The reflection angle is equal, but opposite to the incident angle whereas the transmission angle can be computed using Snell's law 1.2. The δ_x-parameter is the complex dielectric constant of medium x. It is frequency(f) depended property which depends on the dielectric constant(ϵ) and conductivity(σ) of the medium 1.3.[1]

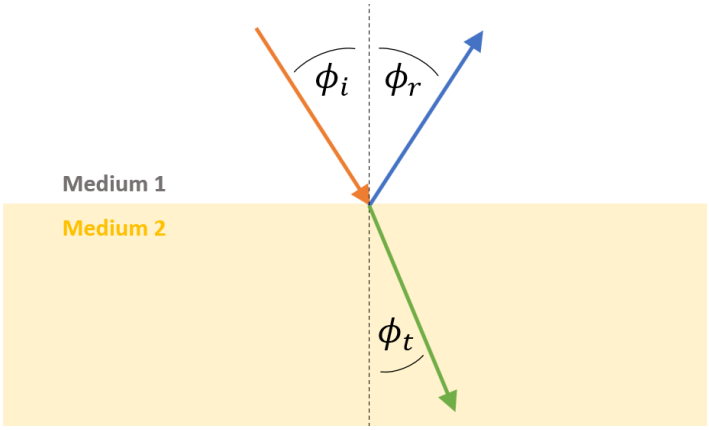

Figure 1.1: Incident Angle ϕ_i, Reflection Angle ϕ_r and Transmission Angle ϕ_t.

$$\frac{\sin\phi_t}{\sin\phi_i} = \frac{\sqrt{\delta_1}}{\sqrt{\delta_2}} \tag{1.2}$$

$$\delta = \epsilon - j\frac{\sigma}{2\pi f} \tag{1.3}$$

The power of the reflected and transmitted radio waves can be calculated by the Fresnell reflection and transmission coefficients.[1] These coefficients are different for transversal electric (TE) and transversal magnetic (TM) waves, in which radio waves can be decomposed. The equations for calculating the reflection(Γ) and

transmission coefficients(T) for the TE waves are given by equations 1.4 and 1.5. Computing the coefficients for the TM waves can be done similarly.

$$\Gamma_{TE} = \frac{\sqrt{\delta_1}\cos\phi_i - \sqrt{\delta_2}\cos\phi_t}{\sqrt{\delta_1}\cos\phi_i + n_2\cos\phi_t} \tag{1.4}$$

$$T_{TE} = \frac{2\sqrt{\delta_1}\cos\phi_i}{\sqrt{\delta_1}\cos\phi_i + \sqrt{\delta_2}\cos\phi_t} \tag{1.5}$$

In reality, the reflected power does not all propagate away from the surface in the specular direction (θ_r), as was depicted in figure 1.1. Surfaces are not perfectly flat, thus incident radio waves reflect back in multiple directions. This is called diffuse scattering. There exist multiple models in which diffuse scattering can modeled.[2][3] Some only apply a correction factor to the reflection coefficient, while others give a power spectral density of the reflected power.

The last propagation mechanism is diffraction. Radio waves travel straight on, but they can bend around objects. This can be visualized by replacing a propagating wavefront by many point source emitting spherical wavelets, according to the Huygens-Fresnel principle. Keller introduced a mathematical description, called geometrical theory of diffraction (GTD), in which diffraction could be modeled.[4] This model is later improved by the uniform theory of diffraction (UTD)[5].[6]

After propagating through an environment, radio waves reach the receiver from different angles, with different delays, phases and amplitudes. At the receiver, all MPCs are summed and due to their differences the superposition can be constructively or destructively. This leads to fast fading or small-scale fading; the received signal strength quickly varies with the position of the receiver.

Channel Simulation

The propagation of radio waves heavily depends on the environment. For reliable channel simulation, standard channel models are thus not fit. Besides measurements, computer simulations are the only possible way to predict the wireless propagation in an specific environment. The types of simulations can be split into two categories: full-wave solvers and asymptotic solvers.

Full-wave solvers solve Maxwell's equations by numerical approaches, such as finite

element method (FEM), method of moments (MoM) or finite-difference time-domain (FDTD). These solvers give accurate results but they are computational complex. Especially for large environments or at high frequencies. These solvers are therefore not very well suited for radio propagation simulation.

Asymptotic solvers do not solve the Maxwell equations, but approach their results in a different manner. ray-tracing (RT) and ray-launching (RL) are two methods to solve electromagnetic problems asymptotically. Both methods describe the radio wave propagation in terms of rays. The lower complexity of asymptotic solvers makes them suitable for radio channel simulations in an end-use environment.

RT simulations try to find every possible path for a ray to travel from a transmitter to a receiver. These rays can reflect via, or transmit through objects along their path. When every path is determined, the corresponding attenuation and delay of each path is computed. The before mentioned reflection and transmission coefficients, as well as path loss are included in calculation. The process of finding all paths from the transmitter to the receiver is computationally less complex, but the complexity increases exponentially with the number of allowed reflections, also called the order of reflections. Also the implementation of diffuse scattering and diffraction is not trivial. RT is still a suitable option to simulate a radio channel in large environments or when high frequencies are used. For radio propagation, multiple channel simulations are required in order the model spatial variations on the channel. With RT, every channel needs to be simulated individually since the paths from transmitter to receiver change with a spatial transition. RT is therefore best suited for simulating point-to-point links.

RL operates in a slightly different manner. Rays are launched from the transmitter at certain angles, with a predefined angular resolution. Each ray represents a small portion of the propagating wavefront. Together, they cover the radiation from the transmitter in all directions. As the rays travel, the area of the wavefront they represent increases. To prevent that rays can represent a very large wavefront area, they can be divided into multiple rays. To determine which rays are received by the receiver, one could include the rays that pass the receiver within a certain radial distance. The main advantage of RL over RT is that RL computes the radio propagation for the whole environment instead of only the rays to a single receiver. It is therefore widely applied for radio propagation simulation or radio channel from one transmitter to multiple receivers[2][7].[8]

Literature Review

RT simulations have proven to be able to yield accurate channel characteristics in many occasions.[7][9] These channel characteristics include mean delay time, rms delay spread, coherence bandwidth and path loss. The accuracy of these characteristics decreases in scenarios without line-of-sight (LOS).[10] This is to be expected as the rays interact more with the simulation environment. Any error in the simulation environment will cause errors in the rays interacting with it. Also, the implementation of the propagation mechanisms plays a larger role in non-line-of-sight (NLOS) scenarios. Path loss, reflection and transmission is fairly straight forward to implement, but diffuse scattering and diffraction are less trivial to implement in a RT simulator.

It is also shown that RT results consist of less MPCs than reality, but it does include the most dominant paths.[11] Once again, this may be due to the implementation of diffuse scattering and/or diffraction, or the choice to neglect these effects.

Although RT and RL are very similar, their results can differ. RL can have a limited accuracy with respect to RL due to the angular discretization of the transmitted rays. RL is less computation costly with respect to the RT algorithm in large simulation areas on the other hand.[7]

The level of detail of the simulation environment required is depend on the set frequency. In the sub-2GHz range, the difference in result with and without modeled furniture is minimal.[10] In the mmWave range however, a very detailed simulation environment is required in order to yield accurate results.[11]

Body shadowing, by for instance a patient, does reduce the wireless performance of wireless body area network (WBAN)[12].[13] The shadowing effect is however significantly reduced in a rich multipath environment.[14] This also shows that reflections via the environment are more dominantly present in the received signal than diffracted waves around the body.

Bodies obstructing the LOS path can be represented by a simplified shape. The diffraction around a cylindrical model is similarly as a human body[15].[16] Close to antenna's, more detail is required, as the body(part) obstructing is more dominantly present in the radio channel than diffraction.**?**

Measurements have shown that bodies passing through dominant MPCs have a significant effect on the received signal.[17] This shows reflection (and transmission) via the environment is a dominant propagation mechanism in indoor environments.

Radio channels can be characterized by a number of parameters. The path loss for instance describes the power difference between the transmitter and receiver. This path loss is distance dependent; a larger separation distance goes along with a higher path loss. The path loss exponent characterizes the increase in loss as function of distance. In free space, the path loss exponent is 2, as we saw in equation 1.1. A Gaussian-distributed random variable can be used to model the impact of large-scale fading to the path loss.[18]

The power delay profile (PDP) of a radio channel describes the received power after a unit pulse is transmitted.[1] From this profile, temporal parameters can be extracted such as the mean delay. The rms delay spread can also be extracted from the PDP. This parameter characterizes the delay dispersion[19].[20] The coherence bandwidth is inversely proportional to the delay spread. The coherence bandwidth characterizes bandwidth in which the channel is relatively constant.

1.2 Goal

Motivation

RT has proven to be a good solution for point-to-point channel simulations. It is much quicker than conventional full-wave solvers, while still being able to achieve accurate channel characterization results. However, propagation mechanisms can be implemented differently among different RT-solvers. RL-simulators prove to be the best solution for wireless propagation simulation, due to their ability to quickly simulate multiple radio channels, and they are thus the best option for simulating of the wireless performance of a patient monitor.

The accuracy of the simulation depends, besides the inclusion of human bodies, on a lot of factors. The level of detail of the environment and its material properties, the use of transmitter and receiver, and the simulator settings can have a large influence. The impact of these factors is situation depended. The factors do not only alter the output of the simulation, they also have an effect on the computational complexity. An increased accuracy often coincides with an increase in computational time. A proper choice has to be made between these, which depends on the required accuracy and the available processing power.

Simulation of a wireless channel is step one. To get an indication of the wireless

performance from the simulated results is step two. A RL-simulator is in theory very well suited for quickly computing multiple radio channels if the environment is static and the transmitter(s) remain stationary. After all, the computation of all the launched rays does not change if these two conditions are met. This makes RL ideal for radio propagation simulation and suited for stochastic feature extraction in a cost-effective way. If the environment is not static due to for instance a patient, one could remove the body's model and integrate its effect by adjusting the radiation pattern of the antenna.

Goal

The goal of the research is to find how a dynamic radio channel, with a mobile patient monitor, in a medical scenario can be efficiently and effectively simulated such that the wireless performance can be evaluated. The radio channel is not static due to movement of the patient wearing the monitor itself, or due to movement by others such as patients, doctors etc. The outcome of a RL simulation of a radio channel depends on many variables and factors. Quantification of the influence of these different factors as well as determining the allowed simplifications is part of the research. The effect of the human body will not be considered, merely the dynamical effect due to movement of a patient. The costs in terms of simulation accuracy due to simplifications should be quantified and weighted against the gained benefit in reduced complexity.

Secondly, the extraction of stochastic features from a simulated dynamic radio channel is to be done in order to evaluate the wireless performance of a communication link. It should be shown that it is possible to evaluate the reliability of a patient monitor in a medical environment based on RL propagation simulations.

Research Questions

- To what extent do simplifications in a ray launching simulator affect the computational complexity and accuracy of radio channel characteristics?
- How can the reliability of a wireless link in the end-use environment be evaluated from ray launching simulations?

Chapter 2

Methodology

This chapter is split into three parts. The simulation method is discussed in the first part. Herein, the operation of RL-simulators is discussed, as well as the workflow of the used RL-simulator. At last, factors causing inaccuracies in the simulations and how they can be mitigated are treated.

In the second part, the measurement technique is discussed. These measurements act as a reference used for validation of the simulation model. How the measurements are conducted is further discussed in chapter 3.

In the last section, the extraction of radio channel parameters from the simulation and the conversion to user experience indicators is discussed. Therefore, simulations of a channel in fictional hospital are solved.

2.1 Radio Channel Simulation Method

There are multiple different ways to simulate radio channels. In this research RL-simulation is used. The general operation of a RL-simulator is discussed in this section. A more detailed description of the workflow of the used RL-simulator is given thereafter.

2.1.1 Ray Launching Simulators

As described in section 1.1, a RL-simulator is an asymptotic solver. It doesn't solve Maxwell's equations, but it simulates the radio wave propagation in terms of rays. Each ray represents a part of propagating wavefront and the field strength is given by a field vector which contains the magnitude and phase of the field. This field vector of the ray is determined by the radiation pattern of the source. As the ray propagates, the wavefront it represents increases in area. The total volume covered by this propagating diverging wavefront is called the ray tube. A visual example of

a ray tube is given in figure 2.1. The size of the ray tube is dependent on the ray density setting of the simulator.

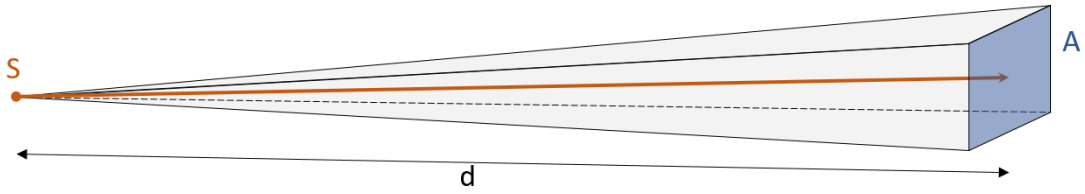

Figure 2.1: Propagation of a Ray Tube from a Source Point *S*. The Cross-sectional Area *A* Increases with Propagation Distance *d*.

The rays interact with a 3-dimensional environment within the simulator. The interaction consists of the aforementioned propagation mechanisms: LOS, reflection, penetration, diffraction and diffuse scattering. The models used of implementing these propagation mechanisms can differ between RL-simulators. Material properties must be assigned to all the geometries in the environment such that these propagation mechanisms can be effectuated.

The number of reflections is restricted to prevent infinite reflections of low power rays. This number, called the reflection order is to be set by the user.

The received signal is acquired by superimposing all ray(tubes) which pass through the receiver. The channel is then described by the difference between the transmitted and received signal. The channel can be simulated for multiple frequency points within the given bandwidth to gain the channel transfer function.

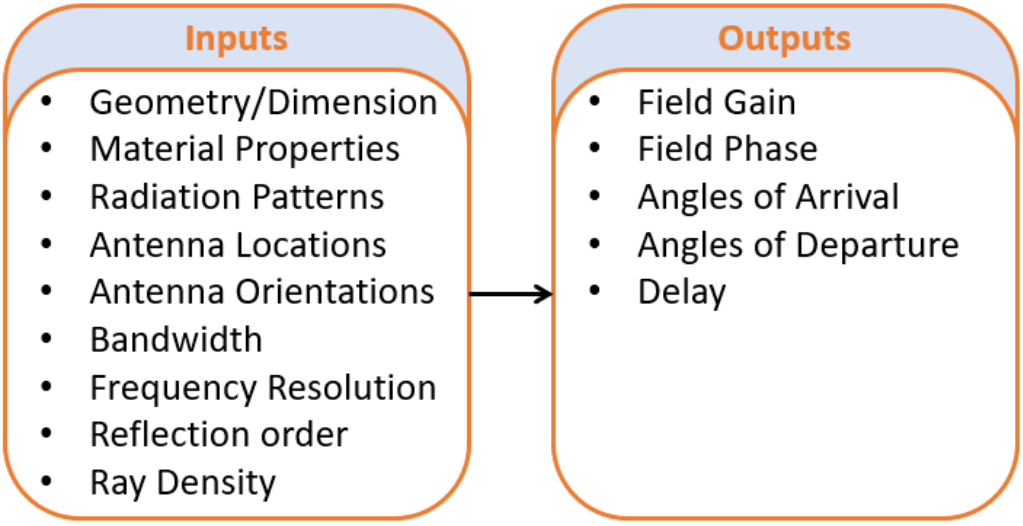

Figure 2.2: Inputs and outputs of a ray launching simulator.

Ansys HFSS SBR+

Ansys HFFS is a 3-dimensional electromagnetic field simulator. Besides a full-wave solver, HFSS offers an ray launching solution called SBR+ (Shooting and Bouncing Rays). Creating the simulation, as well as how Ansys solves the created simulation is briefly explained here.

Creating a Simulation in SBR+:
A simulation consists of two parts: the antennas which act as source and receiver of rays, and the environment. There are several options for sources of rays in the simulation. An incident plane wave can be used as source to simulate the scattering behaviour of an geometrical object. In this research however, antennas are used as sources. SBR+ offers three options to generate an the required radiation pattern of an antenna: parametric antennas, a linked analyzed antenna or importing a far-field data file. The radiation pattern of the transmitter determines the complex field vector of the initial excited rays. Parametric antennas gives the ability to insert basic idealized antennas from which the radiation pattern can be computed by a few parameters, such as a monopole, dipole or horn antenna. The second option allows the user to use a radiation pattern of a custom designed antenna which was previously simulated by the full-wave solver in Ansys HFSS. We call this the hybrid solution since both a full-wave and an asymptotic solver are used to simulate the radio channel. The last option allows the user to import a radiation pattern. Via this option, a measured antenna radiation pattern can be used in the simulations. Each excited ray is given a weight based on the field distribution or radiation pattern of the antenna. The number of excited rays depends on a variable setting called the *Ray Density*, which has as unit rays per wavelength (rays / λ).

2-Dimensional and 3-dimensional geometries can be modeled in SBR+. However, SBR+ does not support volumetric objects as of yet. Therefore, 3-dimensional geometries are in fact a hollow volume covered with 2-dimensional sheets. A boundary has to be assigned to each geometry which determines the reflections and transmission coefficients. Perfect absorbers and a perfect conductor are two possible boundary assignments. For non-conducting materials, a layered impedance boundary can be assigned to a geometry. This type of boundary will be used for all geometries in the simulation. Layered impedances can be either one-sided or two-sided. One-sided layered impedance boundaries will only create reflected rays and no transmitted rays. This boundary assignment can be used if the geometry fully absorbs the transmitted ray or if they geometry is located at the edge of the simulation environment. Two-sided layered impedance boundaries do create transmitted rays. Both types of boundaries can, as the name suggests, can consist of multiple layers. Non-

homogeneous geometries can be modeled this way. Each layer has to be assigned a thickness and a material, with a corresponding permittivity and conductivity. The reflection and transmission coefficients are derived from the thickness and material properties of all layers.

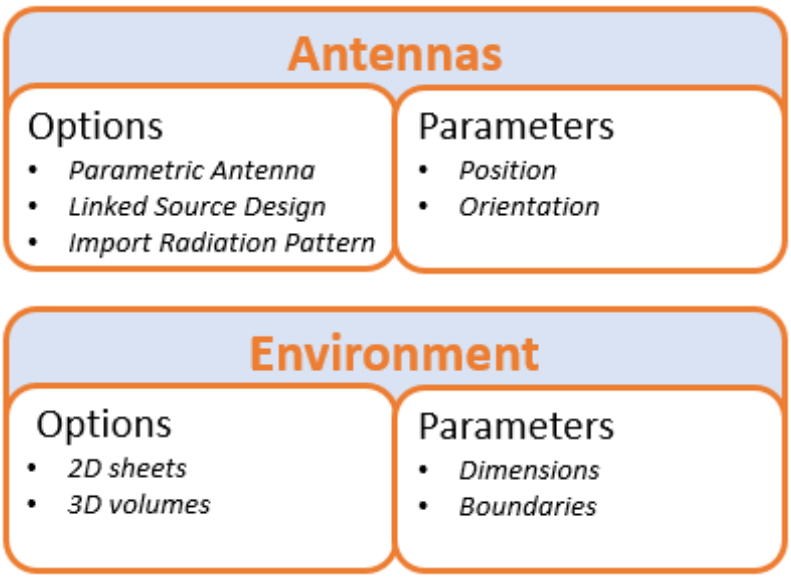

Workflow SBR+:
Rays are launched from transmitting sources. A (complex) field vector is assigned to each ray according to the radiation pattern of the antenna. The propagating ray represents a diverging volumetric ray tube as was shown earlier. During the ray propagation, three things can happen to the ray:

1. The ray propagates a certain distance without hitting a geometry. The ray density drops below the 'Ray Density' setting and the ray is split into two rays.

2. The ray escapes the simulation environment and will be ignored as it is are unable to reflect back to the environment and reach the receiver.

3. The ray hits a geometry. Reflected and transmitted rays will be launched from the hit point. Their respective field magnitude is determined by the Fresnell coefficients. The order of reflections is limited by the variable 'Max Bounce'. If this number is reached, reflected and transmitted rays will not be created.

Diffraction occurs near the edges of the geometries, as was mentioned in section 1.1. As the rays in the simulation travel in straight lines, this effect is not automatically included in the simulation. Therefore, SBR+ has an optional feature called *UTD* which generates extra rays to account for the diffraction at the edges of the geometries.

When a ray impinges a surface of a geometry, the equivalent current is computed at the hit-point on the surface. The equivalent surface current is based on the field of the incident, reflective and transmitted ray together. The equivalent surface currents are used to compute the field at the receiver using physical optics (PO). Ansys uses equation 2.1[21] for this purpose. $\bar{\mathbf{E}_\mathbf{S}}$ is here the scattered electric field at an observation point (the receiver). The integral is taken over $\mathbf{S}'$, which is the intersection between the ray tube and the geometry. $\hat{\mathbf{n}}'$ is the surface normal, and its dot- or cross product with the electric and magnetic field components ($\bar{\mathbf{E}}$) and $\bar{\mathbf{H}}$) respectively) represent the equivalent currents. k and μ_0 are respectively the wavenumber and the free space magnetic permeability. R is the distance between the observer and the integration point on the intersection. This distance is the difference between the position vectors to the receiver ($\bar{\mathbf{r}}$) and the integration point($\mathbf{r}'$), given by equation 2.2. It is important to note that the received signal is thus not based on the rays directly, but via PO.

$$\bar{\mathbf{E}_\mathbf{S}} = \frac{1}{4\pi}\int_{\mathbf{S}'}\left[(\hat{\mathbf{n}}'\cdot\bar{\mathbf{E}})\nabla'\frac{e^{-jKR}}{R} + (\hat{\mathbf{n}}'\times\bar{\mathbf{E}})\nabla'\frac{e^{-jKR}}{R} - j\omega\mu_0(\hat{\mathbf{n}}'\times\bar{\mathbf{H}})\nabla'\frac{e^{-jKR}}{R}\right]d\mathbf{S}' \tag{2.1}$$

$$R = |\bar{\mathbf{r}} - \mathbf{r}'| \tag{2.2}$$

After the field is calculated at the receiver, the actual received signal b at the receiver is calculated using equation 2.3.[21] In this equation $\bar{\mathbf{g}_{\bar{\mathbf{R}}\mathbf{X}}}$ is the complex antenna gain of the receiver and η_0 is the free-space impedance. This equation can be seen as a summation of all scattered fields created by the ray footprints (eq. 2.1). The position of the ray footprint, as seen by the receiving antenna determines angle of arrival. The corresponding complex gain of the antenna is multiplied with the associated electric field contribution of that particular ray footprint using the dot product.

$$\mathbf{b} = \frac{-j\lambda}{\sqrt{4\pi\eta_0}}\bar{\mathbf{E}}\cdot\bar{\mathbf{g}_{\bar{\mathbf{R}}\mathbf{X}}} \tag{2.3}$$

The ratio between the incident signal a and received signal b is given by the complex S21 parameter ($S21 = \frac{b}{a}$). The frequency response of a radio channel can be simulated by repeating this process for multiple frequency points. N_r receivers and N_t transmitters can be introduced into a simulation to yield a S-parameter with dimensions N_r by N_t.

$$S21[f] \in \mathbb{C}^{N_t \times N_r} \tag{2.4}$$

The workflow of Ansys HFSS SBR+ can thus be split into 6 steps, visualized below.

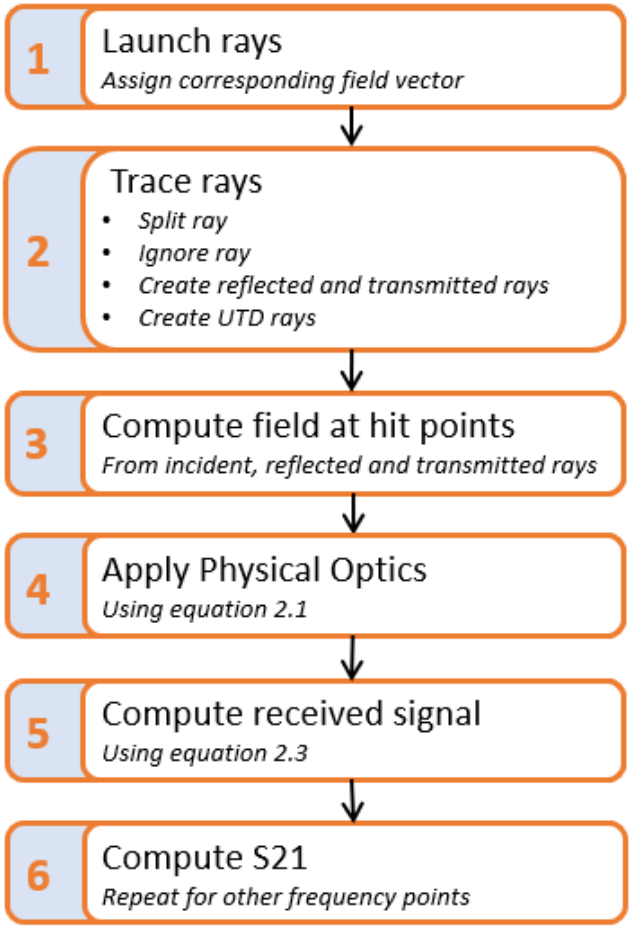

2.1.2 Validation Method of Simulation Model

The simulation model consists of a large set of input parameters from which the accumulated impact on the model accuracy is significant. Therefore, validation of the model is necessary. In this section, the factors causing simulation errors are identified and a strategy is composed to mitigate the potential discrepancies with respect to real life.

Factors Causing Discrepancies

RL-simulators are asymptotic solvers and will thus always contain discrepancies. The radio wave propagation within a certain area is generalized by a ray and its corresponding ray tube even though the radio waves can interact differently to the

environment within such a ray tube.

The limit on the number of reflections set in RL-simulators also induces discrepancies. Generally, higher order reflections contain less power, but completely ignoring them obviously causes errors.

Discrepancies can also lie in the diffraction and diffuse scattering models implemented in the simulator, even if these mechanisms are not dominant in indoor scenarios. SBR+ is able to generate UTD rays (recall step 2 of the workflow) if this options is enables. However, diffuse scattering is only applied in step 4 of the workflow. Non-specular reflections are disregarded in step 2.

A model of an environment will always contain dissimilarities with reality. Structural dissimilarities of certain geometries like inaccurate positioning, orientation, shape or the absences of small objects will cause rays to reflect differently than reality.

Besides the structural discrepancies, the material properties of the geometries can contain mismatches. The properties of a geometry can be estimated based on the type of material. Composition of geometries and their material properties can become quickly cumbersome however, since they can be non-homogeneous and objects can be constructed of multiple parts from different materials.

In the current version of SBR+, volumetric geometries cannot be modeled. These geometries are modeled as 2D sheets. Reflections only take place at the boundary of the geometry, while in reality, rays can penetrate a geometry partially, before being reflected.

The antennas used in the simulations can be a cause of discrepancies as well. Firstly, the position and orientation of the antenna can contain discrepancies. Secondly, the magnitude and phase of the radiation pattern can be inaccurate due to various reasons. Antennas can also be modeled as frequency-independent while they are frequency-dependent.

Mitigation Strategy

Discrepancy factors should be mitigated as much as possible to achieve an as accurate as possible simulation result. Unfortunately, they often coincide with higher

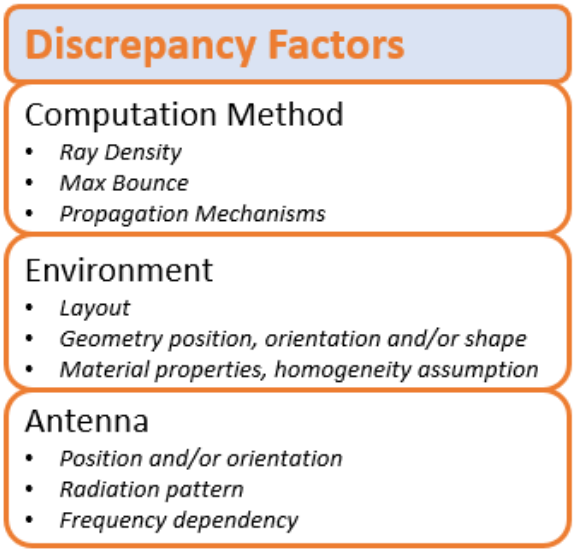

computation complexity. How the cause of discrepancies can be mitigated, and what their expected cost is, is discussed in this section.

A higher ray density and reflection order can increase the accuracy of the simulations. Increasing the ray density will cause rays to split sooner. Subsequently, the new duplicated rays will split again sooner. Therefore is it expected that the computation cost approximately rises exponentially with the ray density. The accuracy improvement by raising the ray density is likely to drop as rays become more and more dense. Therefore, a optimal compromise has to be found between accuracy and computational cost.

Similarly for the order of reflections, a trade-off between accuracy and computational cost has to be made. Increasing the 'Max Bounce' variable will generate more hit points, and thus more calculations are required in steps 2-5 of SBR+. Increasing the reflection order is expected to result in a linear increase in computational cost.

Applying UTD in SBR+ is optional. UTD will generates additional rays within the simulation, originating from the edges of lit geometries. The number of generated UTD-rays depend on the environment. It is expected that computational cost of this options coincides with the accuracy benefit of UTD.

Detailed modeling of the environment obviously leads to lower discrepancies. Creating a detailed model is however not always possible due to the lack of knowledge about the environment and it can be time consuming. 3-Dimensional computer models or drawings of the environment can help creating the environment quickly and accurately, but they are not always possible. Manually measuring the environment

is time consuming and prone to errors and thus not recommended.

Material properties can be based on building plans or estimations. Fortunately, there are lots of tables available containing properties within certain bandwidths.[22] An accurate environment and accurate material properties will, if they can be acquired, enhance the simulation without adding additional computation costs.

Modeling all objects in the environment obviously gives the best representation of reality. However, small objects, or objects far away from the antenna can be excluded without a significant impact on the radio channel. This will not necessarily reduce the computation time, but does simplify the simulation modeling.

Similar to the environment model, antenna models can be simplified to ease the simulation modeling or if no detailed information is available. Ansys has the ability to load source designs containing custom antenna designs. The antenna simulation in this hybrid method is only required to be done once. Importing measured patterns is an option if no antenna design model is available. In this case, the accuracy of the antenna model depends on the measurement data.

2.2 Radio Channel Measurement Method

Measurements are executed which act as a reference in order to validate the simulation model. A radio channel can be measured in the frequency domain, yielding the time-variant transfer function $H(t, f)$ of the channel, or in the time domain, yielding the time-variant impulse response $h(t, \tau)$. The latter option is for the reference measurements. The time-variant impulse response tells how a radio channel behaves to a transmitted pulse at different time instances (see equation 2.5).

$$h[t, \tau] \in \mathbb{C}^{N_r \times N_t} \tag{2.5}$$

Two Decawave modules are used for the reference measurements. The modules have two transmitting antennas and one receiving antenna. It has an ultra wideband (UWB) of 500MHz and a center frequency of 3.5GHz. An example impulse response in of a single radio channel ($N_t = N_r = 1$) is given in figure 2.3.
A detailed description of the operation of the Decawave modules is given in the next chapter, chapter 3.

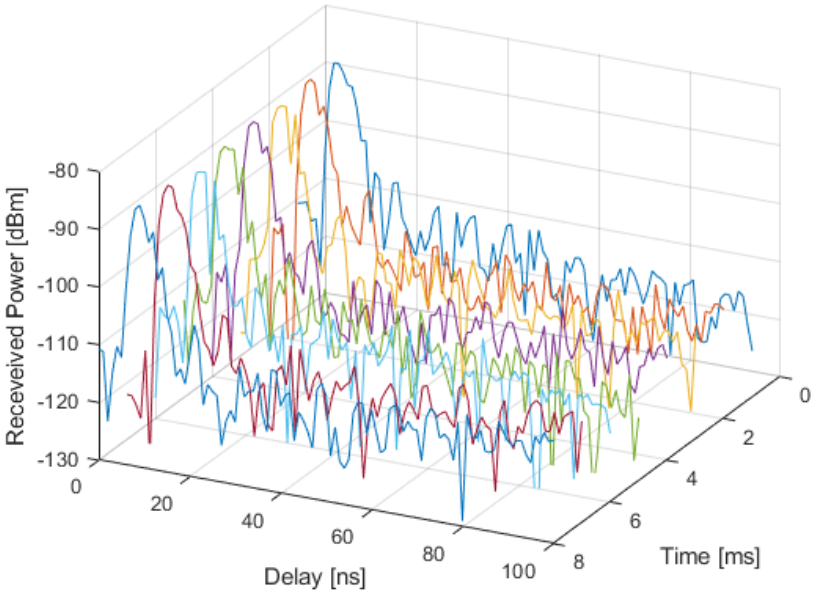

Figure 2.3: Example Impulse Response in dBm of a Channel with a Center Frequency of 3.5GHz, Bandwidth of 500MHz.

2.3 From Radio Channel to User Experience

For validation, the accuracy of the simulated radio channel is quantified via certain key channel parameters. These are described in this section. These parameters will be derived from the simulated channel and measured channel. In the second part, system parameters will be discussed. Together with the channel parameters, they will indicate the performance of the wireless link experienced by a user. A numerical example simulation in an fictional hospital is done for this purpose.

2.3.1 Key Channel Parameters

The simulations and measurements do not yield the same type of output. However, they can both be converted to the PDP P_h. This is straight forward for the impulse response achieved by the measurements. It is computed by averaging over the time-instance t, see equation 2.6. $P_h[\tau]$ and $h_{mea}[t_n, \tau]$ represent the discrete PDP and measured impulse response respectively. N indicates the number of (coherent) time-instances over which is averaged.

$$P_h[\tau] = \frac{1}{N} \sum_{n=1}^{N} |h_{mea}[t_n, \tau]|^2 \tag{2.6}$$

Computation of the PDP from the S21-parameter output of the simulation requires and extra step. The frequency dependent S21-parameter can be seen as the channel time-invariant transfer function $H_{sim}[f]$. The channel is time-invarient since the simulation model completely static; every simulation will yield the same result. The impulse response and transfer function are Fourier pairs and can thus be derived from each other. After applying the IFFT (equation 2.7) to the channel transfer function, equation 2.6 can be used with $N = 1$ due to the time-variance.

$$h_{sim}[\tau] = \mathsf{IFFT}\left(H_{sim}[f]\right) \tag{2.7}$$

From the PDP, three channel parameters can be extracted: The total received power, mean delay and rms delay spread. The latter two parameters described the channel in the time domain, while the former parameter gives information about magnitude of the received power in the PDP. In section 1.1 was described what these parameters tell about a radio channel. The total received power P_r, mean delay τ_m and rms delay spread τ_{rms} are sometimes called the zeroth-, first- and second-order moment of the PDP respectively. Derivation of these parameters from the PDP is shown in equations 2.8 to 2.10[1].[20] τ_{max} is the maximum delay where the power is greater than the noise floor P_n. The power of the noise floor acquired via the measurements, and will be discussed in section 3.1.2.

$$P_r = \sum_{\tau=0}^{\tau_{max}} P_h[\tau] \tag{2.8}$$

$$\tau_m = \frac{\sum_{\tau=0}^{\tau_{max}} \tau P_h[\tau]}{P_r} \tag{2.9}$$

$$\tau_{rms} = \sqrt{\frac{\sum_{\tau=0}^{\tau_{max}} P_h[\tau]\left(\tau - \tau_m\right)^2}{P_r}} \tag{2.10}$$

The coherence bandwidth and rms delay spread are related. The lower boundary of the coherence bandwidth can be approximated via the delay spread by 2.11.[23] The coherence bandwidth gives the bandwidth for which the frequency correlation function is above 0.5.[24]

$$B_{coh} \gtrsim \frac{1}{2\pi\tau_{rms}} \tag{2.11}$$

2.3.2 System Performance

Channel parameters only give information about a specific radio channel, but they do not indicate the behaviour of the system. System parameters are discussed and

how they are correlated to they channel parameters in this section. For convenience, they are split in three domains: the temporal, frequency and spatial domain.

Timing of transmitted symbols is crucial in wireless communication links, even in a static channel. The symbol duration gives the time period in which the same symbol is transmitted. The symbol time determines, in combination with the delay dispersion, if the used bandwidth is considered narrow- or wideband. At the end of symbol duration, when the transmitter send a new symbol, intersymbol interference (ISI) can occur. The old and new symbol overlap at the receiver. A guard interval in-between the symbol transmission can prevent this. The length of the guard interval depends on the maximum excess delay; the part of the signal received with the highest delay. Guard intervals prevent ISI, but are at the same time a period in which no information is transmitted.

A wireless link uses a certain signal bandwidth. The frequency dispersion, indicated by the coherence bandwidth, gives the correlation in the frequency domain. If the signal bandwidth is much smaller than the coherence bandwidth, we have a narrowband channels. Otherwise the channel is wideband. Note the previously stated relation between the delay spread and the coherence bandwidth. Both parameters can determine if the channel is narrowband or wideband via the symbol duration or bandwidth.

Spatial changes will lead to a different fading behaviour of the channel. If a patient were to move around along a path in the hospital, the fading changes over time. How quickly the fading alters determines if the channel is slow fading or fast fading , and the velocity of the patient. The relation between the symbol duration and coherence time will determine if it a slow or fast fading channel.

2.3.3 User Experience

The received power will differ depending on the position of the receiver in the environment. This can be visualized in a heat map. Such a visualization gives a clear overview of the distribution of power over the environment.

The path loss in free space increases exponentially as discussed in section 1.1. In real life, the path loss increases quicker with distance due to shadowing. A path loss exponent can be computed from the simulations, with which the average path

loss as function of the distance can be predicted. Equation 2.12 gives the average path loss in dB L_n, dB for a given distance d and path loss exponent n. Constant system losses L_c are also included.

$$L_{dB} = 10n \log_{10}(d) + L_c \tag{2.12}$$

The path loss is useful to know for link budget calculations. These incorporate all gains and loss in a wireless link. With a known path loss exponent, the maximum range for a required SNR can be computed. Vice versa, the achievable SNR for a given distance can be computed. The latter can be used to calculate the maximum possible information rate, the capacity C (see equation 2.13[25])

$$C = B \log_2 (1 + \text{SNR}) \tag{2.13}$$

A patient monitor does not require to utilize the maximum capacity. Instead, it is likely to communicate some vital signals to a central unit. Therefore, the Bluetooth technology can be used as reference technology, as it is able to exchanging audio data, which requires a similar data rate as transmission of signals from a wireless patient monitor. Bluetooth is also used in body area network (BAN). The bit error rate (BER) gives the probability of an incorrect reception of a transmitted bit. It can be derived from the SNR, for a given modulation scheme. The enhaced data rate (EDR) mode introduced in Bluetooth 2.0 offers an 8-differential phase shift keying (DPSK) modulation scheme by which 3 bits are be communicated by alternating the phase of signal. The lower boundary probability of a bit error can be given by equation 2.14.[26] In the equation M gives the number of symbols in a constellation diagram which is equal to 8 for 8DPSK. Q is the Q-function and γ_b is the energy per bit E_b to noise power spectral density N_0 ratio, given by equation 2.15. The γ_b can be derived from the SNR via equation 2.16. The bandwidth bit period product BT_b is constant in Bluetooth, which is equal to 0.4.

$$P_b \lesssim \frac{2.06}{\log_2 M} \sqrt{\frac{1 + \cos\frac{\pi}{M}}{2\cos\frac{\pi}{M}}} Q\left(\sqrt{\gamma_b \log_2 M \left(1 - \cos\frac{\pi}{M}\right)}\right) \tag{2.14}$$

$$\gamma_b = \frac{E_b}{N_0} \tag{2.15}$$

$$\text{SNR} = \frac{E_b}{N_0 B T_b} \tag{2.16}$$

Similarly, the bit error probability can be computed for the low energy (LE) mode of Bluetooth. This mode uses less power, at the cost of data rate. Its bit error probability can be computed with equation 2.17.[26] The bandwidth bit period product for Bluetooth LE is equal to 0.5.

$$P_b = \frac{1}{2} e^{-\frac{\gamma_b}{2}} \tag{2.17}$$

The BER can never exceed 0.5 since a faulty bit has always 50% chance to be correct given the nature of the binary system.

The last two user experience indicators are the level crossing rate (LCR) and average duration of fades (ADF). The former states how often the received power drops below a certain threshold within a given time period. It can be derived by drawing a path through the hospital environment which a patient could have taken. It is thus depended on the spatial correlation of the channel. The ADF gives the average duration of such a fade. It can be calculated with equation 2.18. The cdf(r) gives the percentage of time, the received power is below the threshold r.

$$\text{ADF}(r) = \frac{\text{cdf}(r)}{\text{LCR}(r)} \tag{2.18}$$

Chapter 3

Measurement Campaign

This chapter is divided in two parts. In the first part, details about the measurement device are discussed. In the second part, the execution of the radio channel measurements is explained.

3.1 Measurement Equipment

Measurements are executed with the commercial Decawave kit. This kit consists of a DWM1002 acting as anchor, and a DWM1003 acting as node. The transmitting Anchor is equipped with two patch antennas whereas the node has a bowtie antenna (see figure 3.1). Both boards have an USB connection for power. Via the same USB connection, the anchor can be controlled with a computer.

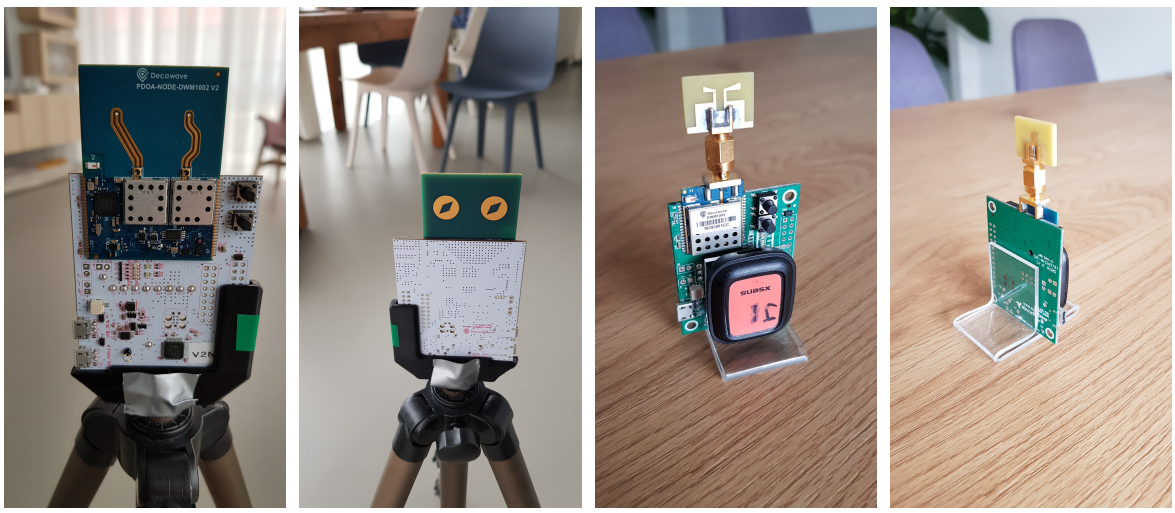

Figure 3.1: Decawave Anchor (Left) and Node (Right).

The Decawave uses the IEEE802.15.4 standard which is suited for a low-data-rate wireless personal area network (WPAN).[27] It is communicating via transmitted

pulses, using UWB to spread out the energy over a large bandwidth. For communication, the Decawave uses a burst position modulation (BPM) and binary phase-shift-keying (BPSK) modulation combination to transmit two bits of information per symbol. However, the Decawave includes diagnostic aids via which the accumulated complex channel impulse response (CIR) data can be accessed. The stored responses are used for the channel measurements.

Instead of transmitting a burst of pulses for communication purposes, the Decawave only transmits a single pulse to accumulate the CIR. The accumulated data includes 1016 datapoints, covering one symbol duration of 1.018 milliseconds. The symbol time is split into four intervals. Pulse bursts can be transmitted in the first and third interval according to the BPM modulation. The second and fourth interval act as guard intervals to separate the first and third interval. In the diagnostic aid mode, a single pulse is transmitted in the third interval.

The received power response in dBm can be estimated from the accumulated data. The estimated received power level can deviate from the actual power level, especially above -85dBm.[28] However, the transmit time is unknown. Fortunately, the Decawave is able to estimate the distance between the antennas, and it is able to detect the rising edge of the first peak. These can be combined to give an estimated transmit time of the pulse.

Parameter	**Value**
Frequency	3.494 GHz
Bandwidth	499.2 MHz
Symbol Time	1.018 ms
Delay Resolution	1.002 ms

Table 3.1: Decawave Characteristics.

3.1.1 Antenna Radiation Pattern

The type of antennas of the two Decawave devices is known, but their radiation pattern is not. Therefore, measurements are conducted to determine these patterns. These measurements are executed in an anechoic chamber located at the High Tech Campus (figure 3.2). The impulse response is measured at three orthogonal planes at an angular resolution of 15 degrees. A computer controller rotating table is used to accurately achieve the angular rotations. All measurements are performed twice; the second time the fixed antenna is rotated 90 degrees such that all polarization are received.. The distance between the antennas is 2.00 meter and the height

is 1.24 meter.

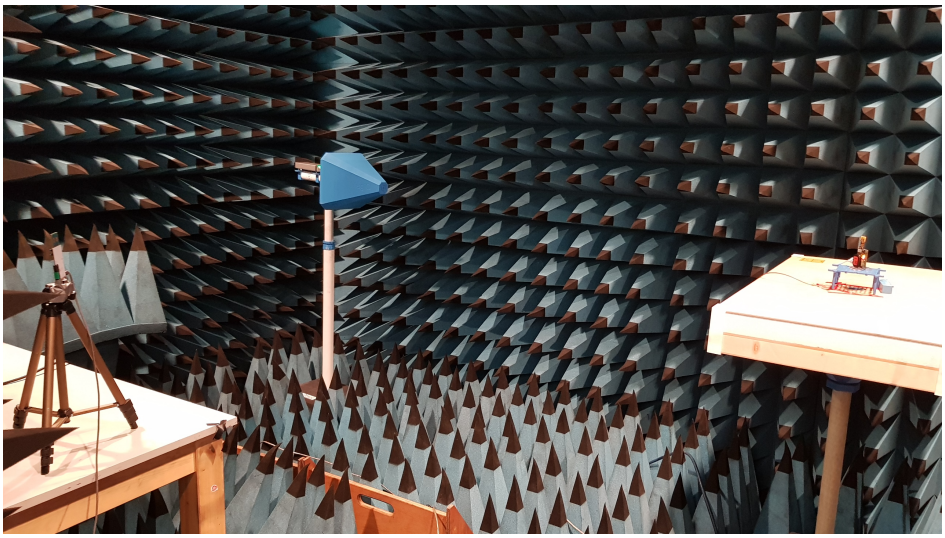

Figure 3.2: The Anechoic Chamber at the High Tech Campus in Eindhoven with the Fixed Antenna (left) and the Rotating Antenna (right).

The received power is based on a 10ns interval within the impulse response. This interval includes only the power received by the direct path. Influence of the radio waves which reflect via the barely present non-absorbing object, will be minimized by applying this interval. The radiation patterns are normalized since the received power is also dependent on the transmit power and path loss. It is important to note that the measured radiation pattern is averaged over the full bandwidth, as the external measuring system was not able to measure or generate the UWB pulse. The measured radiation patterns are given in figures 3.3 and 3.4.The backside of the patch antenna isn't measured as it is assumed that radiation to that direction is negligible due to the ground plane of the antenna.

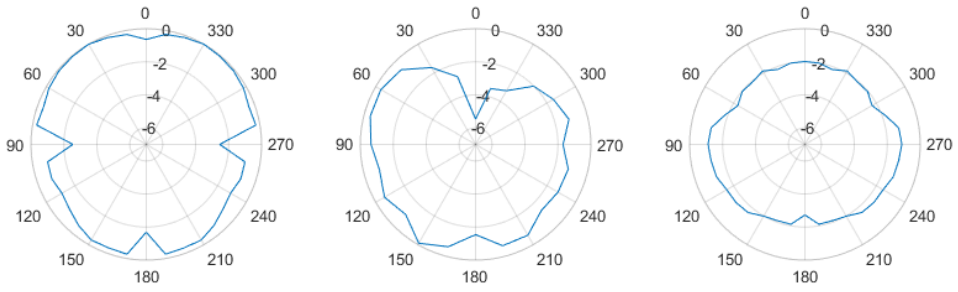

Figure 3.3: Normalized 2D Radiation Patterns of the Node in dB. Horizontal XY-plane(left), Vertical YZ-plane(middle) and Vertical XZ-plane(right).

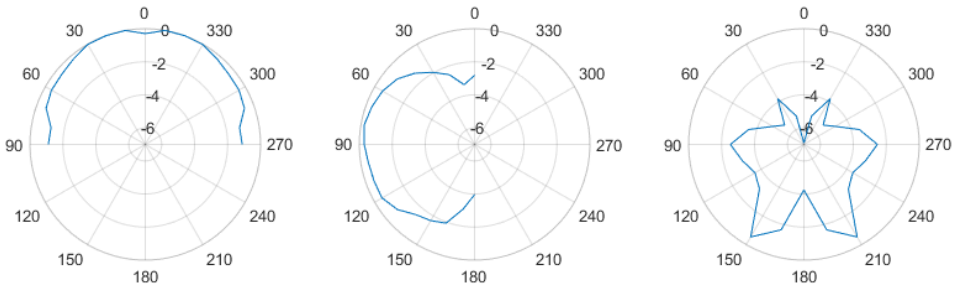

Figure 3.4: Normalized 2D Radiation Patterns of the Anchor in dB. Horizontal XY-plane(left), Vertical YZ-plane(middle) and Vertical XZ-plane(right).

A 3-dimensional radiation pattern is computed by interpolation. The interpolated datapoints are based on the closest measured valued on the horizontal and vertical plane of that particular datapoint. Equation 3.1 is used for the interpolation, where ϕ represents the horizontal azimuth angle, and θ represents the vertical inclination angle. The closest measured points one the horizontal and vertical planes are given by ϕ_{left}, ϕ_{right}, θ_{up} and θ_{down}. The α and β variable determine the weight of the measured points. These are given by equations 3.2 and 3.3.

[h]
$$\begin{aligned} P_r[\phi,\theta] = &\frac{1}{2}\left(\alpha[\phi]P_r[\phi_{left},\theta] + (1-\alpha[\phi])P_r[\phi_{right},\theta]\right) \\ &+\frac{1}{2}\left(\beta[\theta]P_r[\phi,\theta_{up}] + (1-\beta[\theta])P_r[\phi,\theta_{down}]\right) \end{aligned} \tag{3.1}$$

$$[h]\alpha[\phi] = \left|\frac{\phi-\phi_{left}}{\frac{\pi}{2}}\right| \tag{3.2}$$

$$[h]\beta[\theta] = \left|\frac{\theta-\theta_{up}}{\frac{\pi}{2}}\right| \tag{3.3}$$

A far-field data file (.ffd) is created based on these measurement which can be imported in SBR+ for simulation model validation.

The directivity of antenna gives the maximum radiation intensity with respect to the average radiation, see equation 3.4. To calculate the total received power it is not sufficient to sum all measured (and interpolated) points, since spherical areas are not equi-spaced. Points with an inclination angle close to $0°$ or $180°$ are relatively close to each other, while points on the azimuth plane ($\theta = 90°$) are distributed further apart. Therefore, each datapoint is multiplied with $\sin[\theta]$. A constant ζ is added to ensure that on average, the combined multiplication factor equals 1 ($E\{\zeta \sin[\theta]\} = 1$). The resulting directivity with respect to isotropic radiation for both antennas is given in table 3.2.

$$D = \frac{P_{r,max}}{P_{r,avg}} \tag{3.4}$$

$$P_{r,avg} = \frac{1}{4\pi} \sum_{\phi=0}^{2\pi} \sum_{\theta=0}^{\pi} P_r[\phi, \theta] c \sin[\theta] \tag{3.5}$$

Transmitter Directivity (D_t)	2.69 dBi
Receiver Directivity (D_r)	1.72 dBi

Table 3.2: Directivity of Both Antennas.

3.1.2 Equipment specification

Only the maximum transmit power level of the Decawave is known. However, the transmit power can be derived by Friis'transmission equation (in dB scale), given by equation 3.6. The received power P_r can be measured in the anechoic chamber, while the path loss can be computed using equation 1.1. The resulting transmit P_t power yields -31.013 dBm.

$$P_r = P_t + D_t + D_r - L_{\text{path}} \tag{3.6}$$

The noise floor power level is required to calculate the SNR. Fortunately, the first two intervals of the accumulated CIR contain only noise. The noise floor is defined as the maximum value of the noise in those two intervals, given by equation 3.7. Where $-N$ is the first measured value, and $\tau = 0$ is the estimated transmit time of the pulse.

$$P_n = \max(P_h[\tau]) \qquad for \quad -N \leq \tau < 0 \tag{3.7}$$

The highest noise floor level for nine radio channel measurements in the eHealth House is -116.753 dBm. This value will also be used for simulated radio channels, as the noise is not simulated in SBR+ and the frequency and bandwidth are the same.

Transmit Power (P_t)	-31.013 dBm
Noise Power Level (P_n)	-109.3572 dBm

Table 3.3: Power Levels

3.2 Channel Measurements

The reference measurements for the simulation model validation are executed at the eHealth house at the Techmed Centre at the University of Twente. This environment resembles a small house consisting of a living room with kitchen, a bedroom,

a bathroom, a small hallway and a control room. All measurements are conducted in the living room and bedroom, as highlighted by the red lines in figure 3.5. The

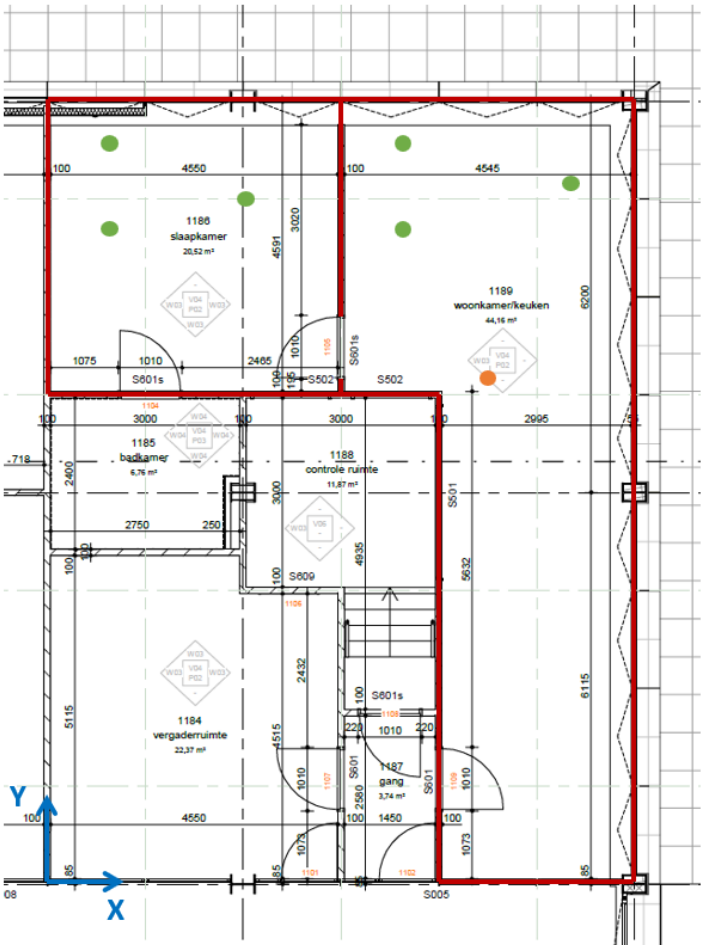

Figure 3.5: Floorplan of the eHealth House. Walls are Highlighted in Red, Transmitter in Orange, Receiver Position in Green.

transmitter is fixed to the ceiling and the1 receiver has nine different positions. The resulting nine different radio channels are labeled. The labels and the corresponding coordinates of the receiver are given in table 3.4. The coordinates of the transmitter are in the table as well. The receiver is horizontally pointing towards the transmitter, while the transmitter is fixed for all measurements. The horizontal orientation angles with respect to the x-axis are given in table 3.4 as well. The validation of the model of the environment, measurements are conducted of the nine radio channels. The receiver is aimed towards the transmitter in all measurements. For the second series of measurements include a human. The letters in the label indicate the posture of the human: G=standing, Y=sitting, B=lying down. These measurements also include rotation. The human and receiver rotate in steps of 22.5 degrees from facing towards the transmitter, to facing away from the receiver.

Label	x [cm]	y [cm]	z [cm]	ϕ [deg.]
TX	700.0	810.9	290.0	135.00
RX-G1	110.0	1040.0	138.0	-21.22
RX-G2	110.0	1140.0	138.0	-29.15
RX-G3	575.0	1140.0	138.0	-69.20
RX-G4	575.0	1040.0	138.0	-61.38
RX-Y1	110.0	1140.0	90.0	-31.62
RX-Y2	575.0	1140.0	90.0	-66.20
RX-Y3	804.5	1050.0	90.0	-29.15
RX-B1	375.0	1011.0	65.0	-69.20
RX-B2	804.5	1050.0	80.0	-66.39

Table 3.4: Coordinates of the Receiver.

Photos of the measurements in the eHealth House and the exact coordinates of the walls are given in appendix A.

An exemplary measured signal is depicted in figure 3.6. The received signal of the 2×1 channel is shown, as well as the measured noise floor. The channel characteristics extracted from the measured radio channels will be used to validate the simulations in the next chapter.

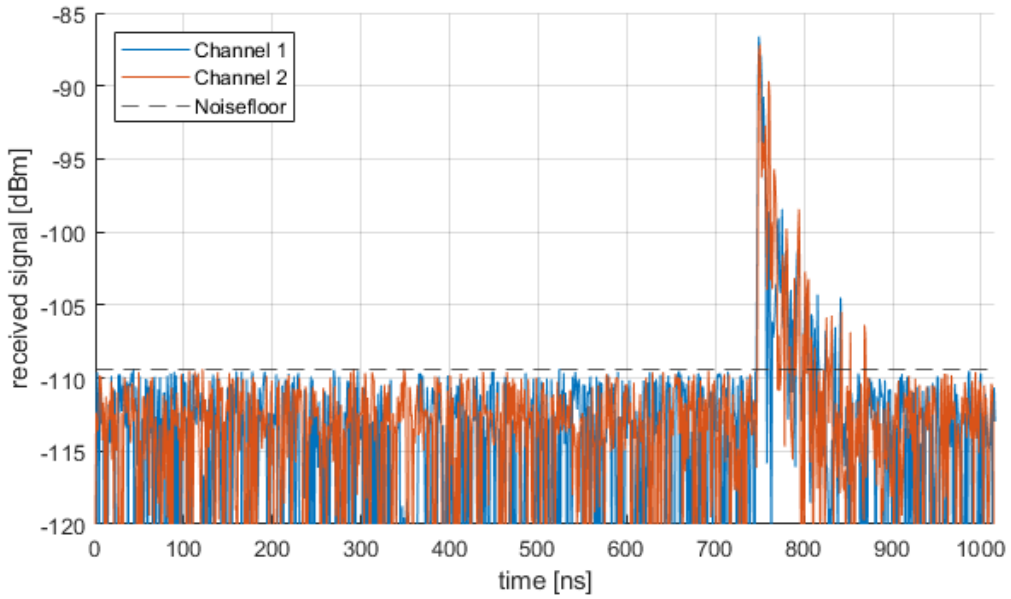

Figure 3.6: Example received signal of the measured 2×1 radio channel.

Chapter 4

Results & Analysis

This chapter is split into four section. First, the validation of the simulation model is discussed, whereby the reference measurements were used. The acquisition of data for a statistical analysis of the radio propagation in a hospital environment is thereafter described. Finally, the user experience of a wireless link by for instance a patient is given, followed by a brief summary.

4.1 Simulation Model Validation

The eHealth House environment is utilized for simulation validation. In the previous chapter is discussed how the reference measurements were conducted. These measurements of the radio channels will be compared to their simulated channels. An initial simulation model of the eHealth House is herefore created.

Initial Model

The dimension of the rooms of the environment are based on a 2-dimensional floor plan in combination with the measured height. The global shape of the large furniture is also simulated. The material properties of the used materials are estimates, where the type of material is based on visual inspection of the environment. The permittivity and conductivity values are gained from the building material properties given by the International Telecommunication Union.[22] These values are given in table 4.3.

Parametric antennas are used as transmitter and receiver. A slot antenna with ground plane is used as transmitter and a halve-wavelength dipole antenna is used as receiving antenna. The dipole antenna is chosen as the bowtie antenna design is based on a dipole. Both patterns have a reasonably omnidirectional radiation pattern though it is expected that the dipole is more frequency dependent than the

Material	$\mathrm{Re}\{\epsilon_r\}$	σ [S/m]
Brick	3.75	0.0380
Glass	6.27	0.0192
Concrete	5.31	0.0892
Ceiling Board	1.50	0.0021
Wood	1.99	0.0180

Table 4.1: Material Properties Used in the Simulation Model.

bowtie. A slot antenna is used, as its pattern matches the pattern of the Decawave's patch antennas the best. All radiation patterns are shown in figure 4.1 and 4.2.

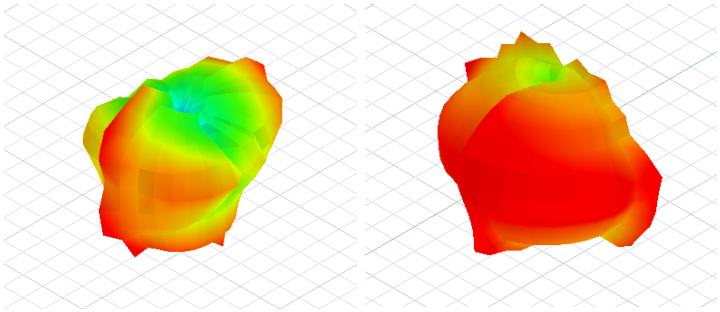

Figure 4.1: Radiation Patterns Decawave: Node(left) and Anchor(right).

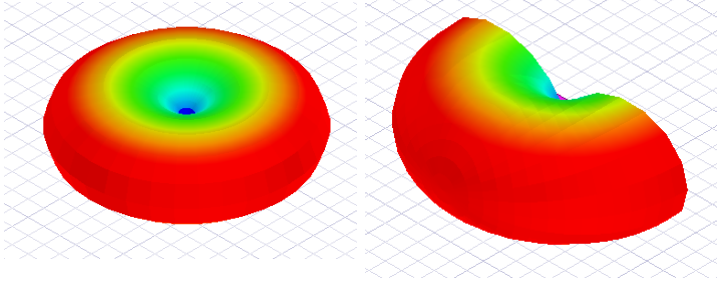

Figure 4.2: Radiation Patterns Parametric Antennas: Dipole Antenna(left) and Slot Antenna(right).

As discussed before, two important settings in SBR+ are the reflection order - called *Max Bounce* in SBR+ - and *Ray Density*. To find the effect of these values on the radio channel and the computation time, a radio channel in the eHealth House environment is simulated for different values of these parameters.

First, a sweep through the*Max Bounce* parameter is performed. The complex valued S21-values within a 500MHz bandwidth frequency sweep are compared to those of a benchmark frequency sweep with a (high) *Max Bounce* which is set to a maximum of 6 reflection. The error is defined as the difference between those S21-values (see equation 4.1). $S21_x[f]$ is the complex S21-parameter at frequency f with *Max*

Bounce set to x. A 500MHz bandwidth in combination with a center frequency of 3.5GHz is chosen as it is equal to the operating frequency of the Decawave. The results are shown in left two graphs of figure 4.3. The top plot show a box-plot of the 200 frequency points within the 500MHz bandwidth. A exponential decay in $|\Delta S21|$ is visible whereas a linear increase in computation time can be seen in the bottom graph. Based on these results, an optimal value of 4 for the *Max Bounce* parameter is chosen, as the discrepancy in radio channel is little, and the simulation time tolerable.

$$|\Delta S21[f]| = |S21_6[f] - S21_x[f]| \tag{4.1}$$

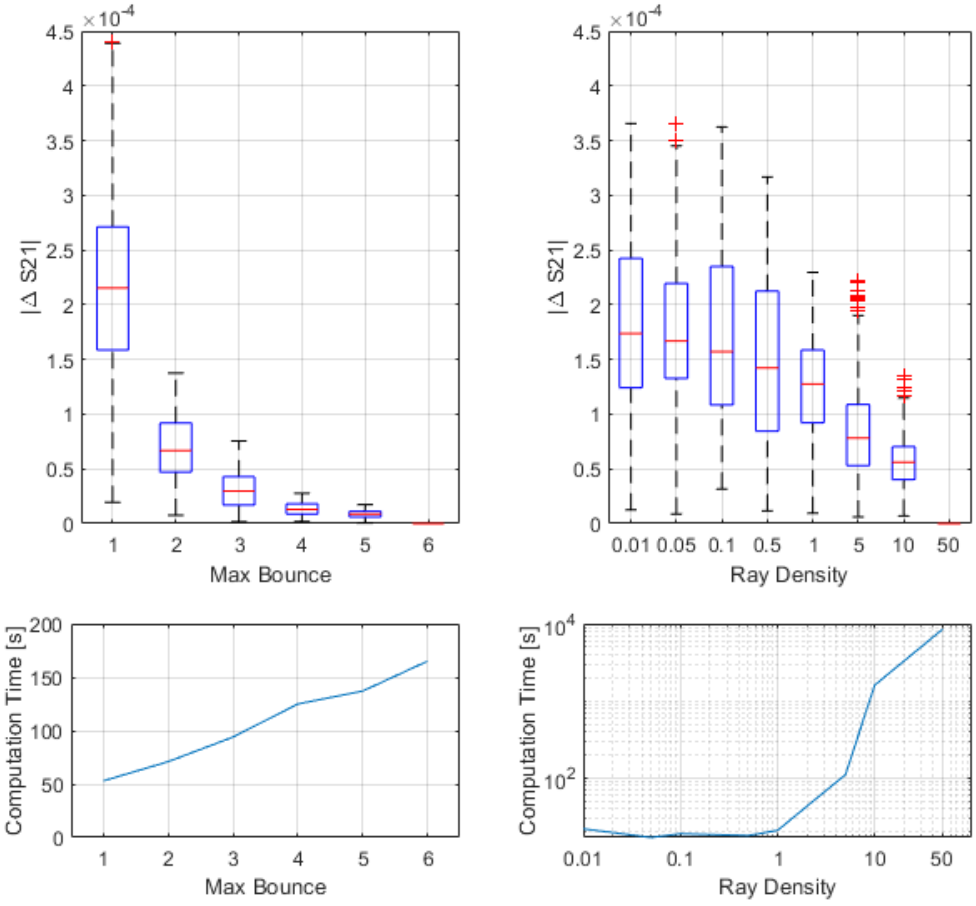

Figure 4.3: Distribution of Errors for 27 Small Positions Changes.

For te *Ray Density* parameter, a benchmark value of 50 is used. The discrepancy with respect to this value, as well as the computation time is shown in the right two graphs of figure 4.3. The computation time is very small for *Ray Density* values

below 1. It is approximately constant at ± 20 seconds. For these values, the simulation time is not dominated by ray propagation computation, but by other simulation steps such as loading the radiation patterns etc. Above 1 though, the expected exponential increase in time can be seen. The discrepancy in S21-values also decays above a *Ray Density* of 1. Both trends considered, a *Ray Density* of 10 is picked as appropriate value, since the simulation time is acceptable. Quick simulations of multiple channels would not be possible anymore by values closer to a *Ray Density* of 50.

Performance Metrics

The correspondence to the measured radio channels is measured by the errors of four channel parameters. These parameters are the total received power, mean delay, rms delay spread and coherence bandwidth. The root-mean-square error (RMSE) of these parameters are used as performance metric. Calculation of the RMSE of the mean delay, and similarly with the other parameters, is done using equation 4.2. In this equation $N = 9$, since nine radio channels have been simulated and measured. The RMSE is thus based on the discrepancies of all nine radio channels. The average simulation time (t_{sim}) of a single radio channel is given in the table as well.

$$\text{RMSE}_{\tau_m} = \sqrt{\frac{1}{N} \sum_{N} \left(\tau_{m,mea} - \tau_{m,sim}\right)^2} \tag{4.2}$$

Discrepancy Mitigation

The discrepancies between the simulated channels and the measured channels are tried to be minimized in several steps. The simulation time is hereby monitored in order to indicate the computational cost of potential improvements.

At first, the UTD option in SBR+ is enabled to add the ray diffraction effect to the simulated channel. The RMSE-values and the simulation time of the initial model without UTD enabled, and the model with UTD enabled are given in table 4.2. In the table we see no improvement in the errors and timing values when the UTD option is enabled. The small time increase implies that the number of additionally generated rays is very limited. The small changes in the RMSE's confirm this statement. This also proves that diffraction is not a dominant propagation mechanisms in this scenario, as was expected. The benefit from this option is thus proportional to the dominance of the mechanism in the scenario, which is also correlated to the computational cost.

	RMSE$_{P_r}$ [dB]	RMSE$_{\tau_m}$ [ns]	RMSE$_{\tau_{rms}}$ [ns]	RMSE$_{B_{coh}}$ [MHz]	t_{sim} [s]
Initial Model	16.784	19.617	13.667	5.293	173
UTD Enabled	16.929	20.142	13.858	5.330	175
Imported Radiation Pattern	8.998	2.060	3.957	3.941	196
Tweaked Materials	6.532	2.931	3.879	4.604	198

Table 4.2: RMSE and Simulation Time.

Secondly, the parametric antennas are replaced by the measured radiation patterns, which are imported. The errors reduce significantly by using the imported radiation patterns as can be seen in the table. The imported pattern does not include phase information, thus they do still not perfectly match their real life counterparts. Adding phase information to the radiation pattern is assumed to further decrease the discrepancy. Also, the simulation time did only increase by 21 seconds per radio channel. Using imported antenna patterns does not generate additional rays. Only alter the (initial) field vector assigned to the rays is altered. The additional time required presumably originates from loading the pattern file and will thus likely not scale with the number of rays (in contrast to the *Max Bounce* and *Ray Density* parameters).

The initial material properties of the simulation environment are estimates, based on homogeneous building materials. In reality, cables and pipes will run though the walls, floor and ceiling. They are likely made of metals, thus a higher reflectivity is expected. The same can be said about the coating on the glass wall. In an attempt to decrease the discrepancy, the material properties can be adjusted to get a better agreement. To do this, the environment is to be split into six material categories: three different of walls, a floor, a ceiling and the furniture. Each material category has two material properties, resulting in 12 unknowns. Finding an optimal value for all of those variables at the same time is impossible since it leads to an extremely large number of required simulations. Therefore, appropriate permittivity and and conductivity values are found category by category by sweeping over possible values. The radio channel with receiver position label *RX-G4* is used since it has LOS and is closest to the transmitter. The adjusted conductivity and relative permittivity values are generated by equations 4.3 and 4.4. Parameters a and b have values of respectively $[-2, -1, 0, 1, 2, 3, 4]$ and $[0.0, 0.5, 1.0, 1.5, 2.0]$.

$$\sigma_{new} = 10^{a}\sigma_{ini} \tag{4.3}$$

$$\epsilon_{r,new} = 1 + b\,(\epsilon_{r,ini} - 1) \tag{4.4}$$

First, the properties of the glass wall are updated. This wall is selected at first, since the wall has a window frames, a sunscreen, presumable coated glass and it is located directly behind the receiving node. The second material category is the concrete ceiling. The transmitting anchor is close to the ceiling, thus lots of rays will reflect via the ceiling. Finally, the material properties of the concrete ceiling and brick partition wall in-between the living area and the bedroom are adjusted. The floor is most likely reinforced concrete, and electricity wires will run through the wall. The initial material properties could therefore be invalid. The remaining materials are left out of this analysis, since they have little presence in area around the transmitter and receiver. Also, the remaining error after four material categories are updated is likely not due to invalid material properties of these materials, but due to other modeling errors and/or simplifications in the environment.

The best a- and b-values found for the four materials are shown in table 4.3. These values are chosen based on the error in the total received power, mean delay and rms delay spread of the radio channel. Attention has been given that a single material does not compensate for other errors and thus material properties closer to the initial value have preference.

Material Category	a	b	Error: P_r	Error: τ_m	Error: τ_{rms}
Glass Wall	2	1.0	1.479 dB	2.061 ns	7.626 ns
Ceiling	1	1.0	1.330 dB	1.772 ns	7.404 ns
Floor	1	0.0	0.722 dB	0.964 ns	6.217 ns
Partition Brick Wall	-1	1.0	0.874 dB	0.593 ns	5.630 ns

Table 4.3: Step-wise Errors when Updating Material Properties.

In the table we see that the errors can be reduced by changing the material properties. Especially the power levels can be tweaked by the material properties, as the variables determine the reflection and transmission coefficients. The mean delay and delay spread can be tweaked less easily since they depend more on the reflection position instead of the coefficients. If we compute the RMSE of all nine channels with the new material properties, we see do not see a clear improvement in accuracy. The RMSE of the total received power has dropped, as the wall, ceiling and floor have become more reflective. The other three parameters show barely any improvement and even have higher errors.

This proves that material properties can hardly by optimized by tweaking them one by one. It takes lots of time to simulate the channel with lots of potential new values and the resulting improvement is little. It is also not certain that the new material properties are actually more accurate, or if they compensate for other modeling errors.

Small position mismatches of the antennas can cause multiple MPCs to add destructively at the receiver instead of constructively, and vice versa. Therefore, the position of the receiver is tweaked in order to find an optimal position. A total of 27 positions close to the original receiver have been simulated. The maximum position change is set to $\lambda/2$ such that positions with a low spatial correlation are included. The resulting distribution of the three errors is given in figure 4.4.

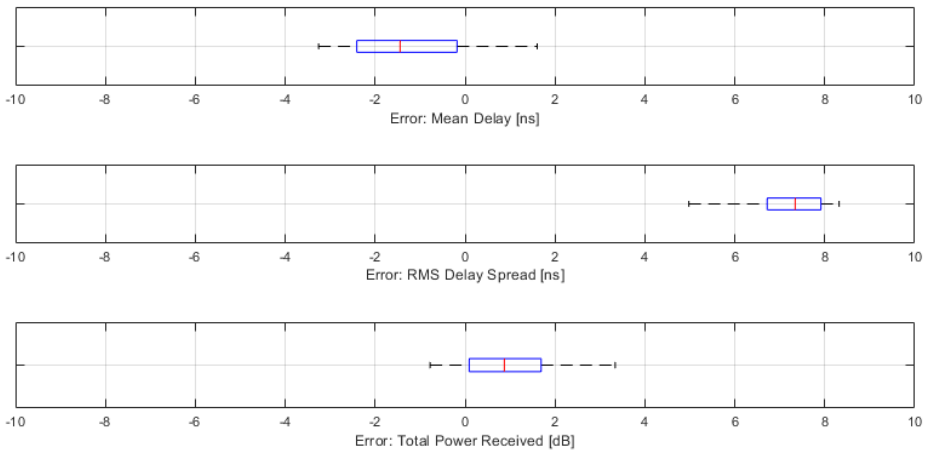

Figure 4.4: Distribution of Errors for 27 Small Positions Changes.

As expected, the figure shows that the error values changes for small position alterations. The mean of the errors for the mean delay and total received power are both close to 0. However, there is no position for which both these errors is low. The graph does show that position mismatches of the receiver, and also the transmitter, can be the cause for the remainder of the errors of these parameters.

This cannot be said about the delay spread. The remaining error for this parameters cannot be fully assigned to a receiver position mismatch. The simulation thus contain additional factors which cause this inaccuracy. These factors can be transmitter position mismatches or errors is the environment's simulation model.

If we compare the PDP's of the simulated and measured channel, see figure 4.5, we see that the delay of the most dominant MPC's correspond. The power of those MPC's does corresponds as well in the initial phase of the PDP (note that the noise-floor is emitted in the simulation PDP.). However, the power fades quicker for the simulated PDP. This steeper line can be perceived in all 9 radio channels. The power lost over time must be a result of power loss in the environment, since the initial peak corresponding to the LOS component is approximately equal. This implies that either too much power is lost via rays which penetrate through the outer walls, leave the simulation environment and are disregarded, or that a significant amount of power is lost after the maximum reflection order is achieved. Presumably, it is the former case since the higher power loss immediately starts after the LOS component's peak when the *Max Bounce* limit is hardly reached by any ray. The increased power loss due to outward penetration is likely a result of improper material properties.

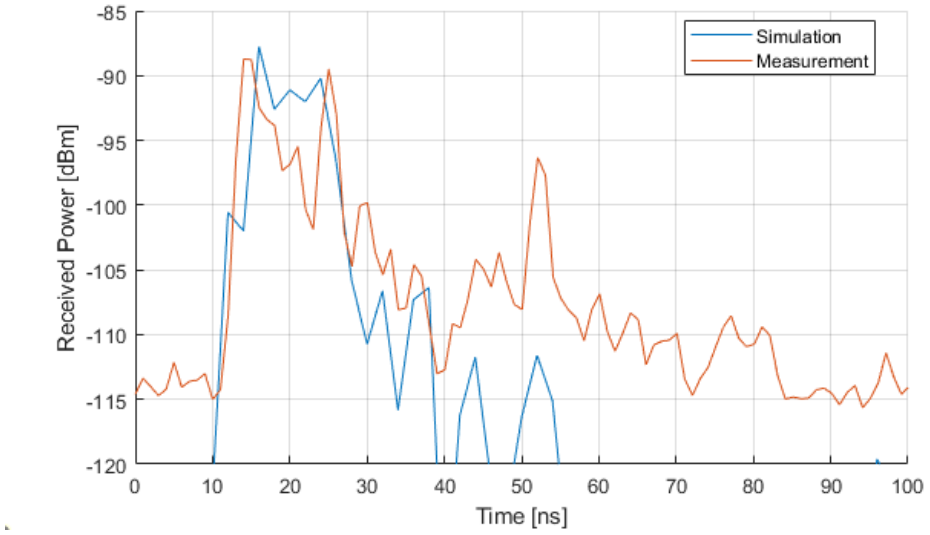

Figure 4.5: Simulated and Measured PDP of the 'G4' radio channel.

To summarize the simulation validation: key channel parameters can be accurately simulated with SBR+. Especially the received power and mean delay parameters yield very accurate results. The remaining discrepancies of the rms delay spread and coherence bandwidth are largely attributable to errors in the environment model. The PDP show a steep decline of power in the simulation case, which is likely due to incorrect material properties. Finding the proper values for these materials is however cumbersome as was shown.
Besides the accuracy on the environment model, the simulation accuracy is large influenced by the antenna's used in the simulations. The cost of the simulation in

terms of the simulation time is mostly determined by the simulation settings, especially the *Ray Density*.

4.2 Statistical Channel Acquisition

Ray launching simulators are best suited for radio propagation simulation since they have a low computational requirements and the ray propagation is independent of the receiver position. Therefore, a large number of radio channels can be simulated efficiently, in theory. Unfortunately, every radio channel is simulated individually in SBR+, even though step 1 to 3 of the workflow of SBR+ remain the same for every simulated radio channel (recall section 2.1.1).

Nevertheless, 128 radio channels are simulated in a fictional hospital (figure 4.6). The hospital consists of 6 rooms and a hallway. The path loss is assumed to be dominated by blockages and reflection off the walls. Therefore, no furniture is modeled. The transmitter is located, near the ceiling in one of the middle rooms, close to the doorway. A central position is chosen to simulate the coverage in the six rooms. The applied material properties for brick (walls), concrete(floor and ceiling) and glass(windows) are those given in table 4.3.

The 128 receiver positions are spread evenly in the entire environment at a height of 1.38cm. This height is approximately the height of a patient monitor when a patient is standing or walking. The environment model is shown in figure 4.6.

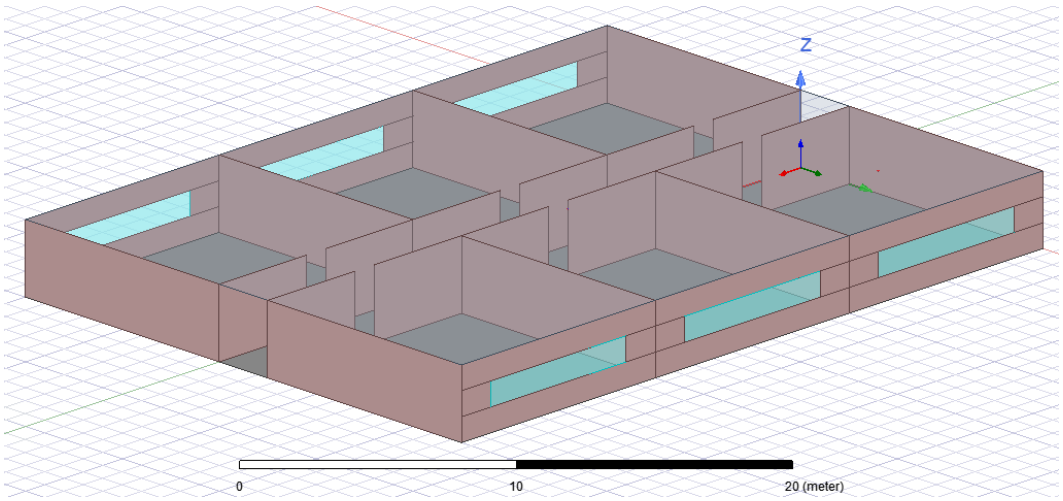

Figure 4.6: Hospital Model.

4.3 Link Performance and User Experience

The parameters used for validating the simulation model are not directly experienced by the user. Instead, the users experiences as successful connection, or a too slow or failed connection. The fail rate of the wireless link and the effect of temporal and spatial transitions on the link connection will be noticed by the user. Indicators hereof are derived in this section.

Path Loss

The fading of a radio channel changes when a patient moves around. The variance in the path loss is visualized in a heat map (4.7). The transmitter is located in the middle room at the right side, visualized by the red dot. It is clearly visible that receiver points with LOS to the transmitter experience a significantly lower path loss. Only a single point in the room of the transmitter itself experiences a path loos higher than 55 dB. Presumably due to destructive addition of multiple MPC's. The top and bottom left rooms experience the most path loss as rays can only reach these rooms via multiple reflections and/or by passing through multiple walls.

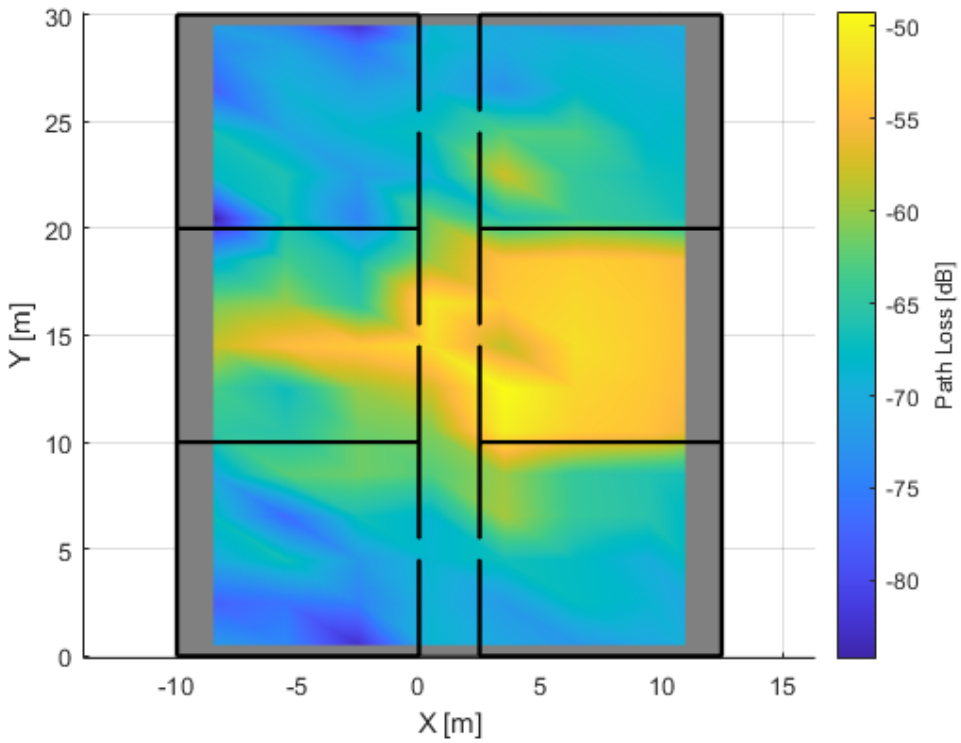

Figure 4.7: Heat Map of the Path Loss. Red Cross Denotes the Transmitter Position.

The path loss as function of the distance can be modeled, as we saw in equation 2.12. The path loss exponent n and constant loss L_0 in this function can be found if a sufficient amount of datapoints is known. The optimal values for these two unknown can be found via cost function. The cost C_p, when the receiver is at position index p, is given by equation 4.5.

$$C_p = L_{dB}(d, n, L_0) - L_{p,sim,dB} \tag{4.5}$$

L_{dB} is the path loss calculated using equation 2.12 and $L_{p,sim,dB}$ is the simulated path loss. This is calculated with equation 4.6. The distance d of the simulated channels can easily be calculated from the position coordinates of the transmitter and receiver.

$$L_{p,sim,dB} = 10 \log_{10} \left(\sum_f |S21_p[f]|^2 \right) \tag{4.6}$$

The n and L_0 for which the average cost $E\{C_p\}$ of all positions is lowest are $n = 2.760$ and $L_0 = 38.085$ dBm. The path loss with these two acquired values gives an average path loss for a given distance. A Gaussian distributed random variable can be added to the path loss equation which models the variation of the path loss. The path loss is then given by:

$$L_{dB} = L_0 + 10n \log_{10}(d) + \chi(\mu, \sigma) \tag{4.7}$$

The mean μ of the random variable χ should be 0 if the pathloss exponent n and constant losses L_c are accurate. The standard deviation σ can be acquired by the distribution of the cost function C_p. This yields a standard deviation of 4.690. Note that this is only a standard deviation of the simulated channel samples which has a limited size.

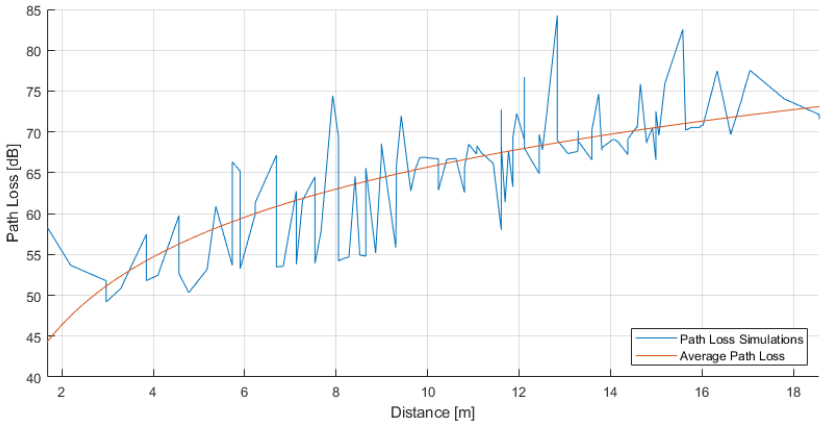

Figure 4.8: Average Path Loss and Simulated Path Loss versus Distance.

Variable	Value
n	2.760
L_c	38.085 dB
μ	0
σ	4.690

Table 4.4: Path Loss Model Variables.

Bit Error Rate

The BER can be calculated from the signal-to-noise ratio (SNR). An upper limit for the BER can be set, by setting a required minimum bitrate. An audio signal is taken as reference as its signal has similarities to a signal measured by a patient monitor. An bitrate of 160 kbps is taken as minimum.

The Bluetooth technology is used as was previously mentioned. Besides the different available modulation schemes, also various options are available in the physical layer (PHY). Three different combinations are compared with each other, which are shown in Table 4.5. Besides the classic *EDR* Bluetooth variant, two newer LE variants are applied as well. *LE 1M* is the original low energy variant of Bluetooth. The coded variant also includes forward error correction (FEC) which allows the receiver to correct falsely received bits. The maximum bitrate is reduced due to the required error correction bits.

Bluetooth Type	Modulation	Maximum Bitrate
EDR	8DPSK	3 Mb/s
LE uncoded	GFSK	1 Mb/s
LE coded (S=2)	GFSK	500 Kb/s

Table 4.5: Bluetooth Types.

The simulated path loss of all channels can be combined with the computed power levels of section 3.1.2 to yield the SNR-distribution (see figure 4.9). In the histogram we see a combination of two bell-shaped curve. The small bell with is center between 30 and 35dB originates presumably from the channels where the receiver was placed in line of sight of the transmitter. The large bell with its center between 15 and 20dB presumably originates from the NLOS channels.

The PER can be derived from the SNR with equations 2.14 and 2.17. Note that equation 2.14 only gives an lower limit for the BER. Wireless communication uses packets to transfer data. Therefore, the BER has to be converted to packet error

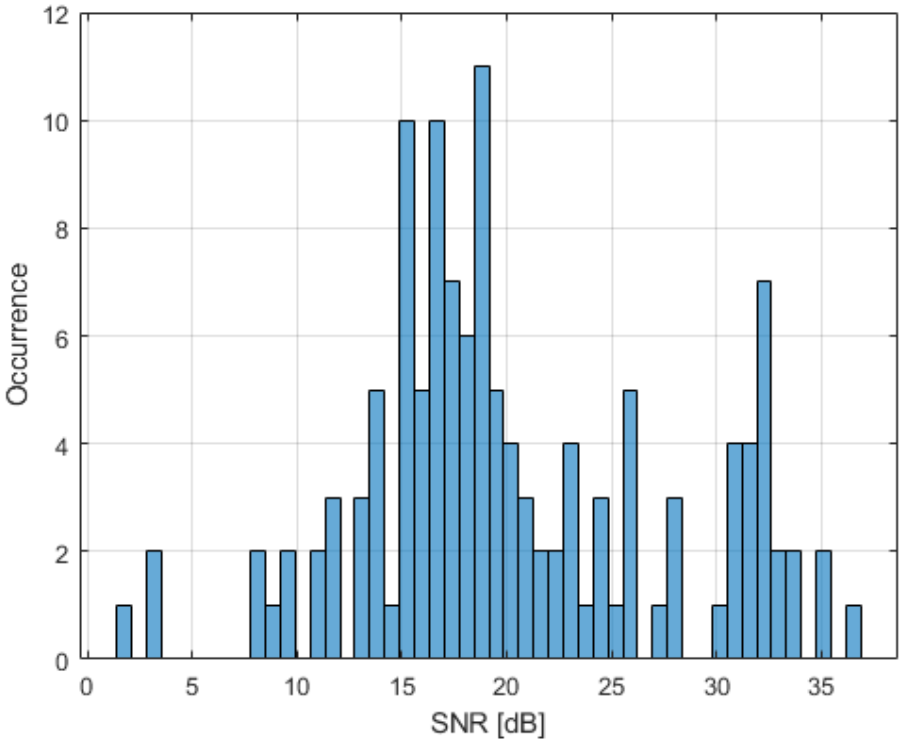

Figure 4.9: Distribution of the Simulated SNR-values.

rate (PER). Normally, packets fail is there is a false bit in it. Implementation of FEC in the coded variant of Bluetooth LE has the ability to correct some of these errors. The PER, or the probability of a packet error, for the uncoded variants without FEC and the coded variant is given in equations 4.8 and 4.9 respectively.

$$P_{p,\text{uncoded}} = 1 - (1 - P_b)^s \tag{4.8}$$

$$P_{p,\text{coded}} = 1 - \left((1 - P_b)^8 + 8P_b(1 - P_b)^6\right)^{\frac{s}{8}} \tag{4.9}$$

The s represents the packet length. For simplicity, we take an equal packet length for all variants. Equation 4.8 is easy to understand. $(1 - P_b)$ gives the probability of a successful bit transmission. Successful bit transmission has to happen for all bits in a packet for a successful packet transmission, therefore the power s.

To understand how the second equation was formed, some information about the encoding for the error correction is needed. therefore, the illustration in figure 4.10 is given. For every bit of information given in the top row, two bits are transmitted (hence the halved maximum bitrate) depicted in the bottom row. The values of the transmit bit-pair in the bottom row depend on the information bit in the top row and

its three predecessors, shown by the letter *A*. Vice versa, the value of a single information bit is thus used as an input to determine the values of four bit-pairs, shown in red. At the decoder, four bit-pairs are decoded to obtain the information bit. If a bit error occurs in one of the bit-pairs of *B*, it can be corrected if the other three bit-pairs are faultless. In equation 4.9, the $8P_b(1-P_b)^6$ term, gives the probability that a bit-pair has one or two errors while the other 6 bits are correct.

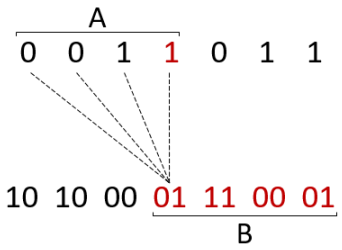

Figure 4.10: Illustration of the Encoding. The Top Row Represent the Information Bits. The Bottom Row Represent the Transmitted Bit-Pairs.

The PER has impact on the achievable bitrate. The throughput T can be given by equation 4.10, where R_p is the packet rate given by equation 4.11. In this equation S is the bits per symbol which is depends on the modulation scheme, R_{sym} is the symbol rate and s is the packet length. The symbol rate in all cases is 1×10^6 symbols per second.

$$T = (1 - P_p)sR_p \tag{4.10}$$

$$R_p = \frac{SR_{sym}}{s} \tag{4.11}$$

Figure 4.11: overview.

Combining the equations, the relation between the throughput and the BER can be derived. This relation is shown in figure 4.12 for all three considered Bluetooth variants. The minimum throughput of 160 kbps is also shown in the figure by the dotted line. For very low BER, the maximum bitrate given in table 4.5 can be achieved as is expected. At higher BER, the throughput will drop to eventually 0 bps due to higher packet loss. For the coded variant, this drop is shifted to the right due to

the error correction code. The maximum allowed BER for the three variants can be found by the intersection with the dotted line.

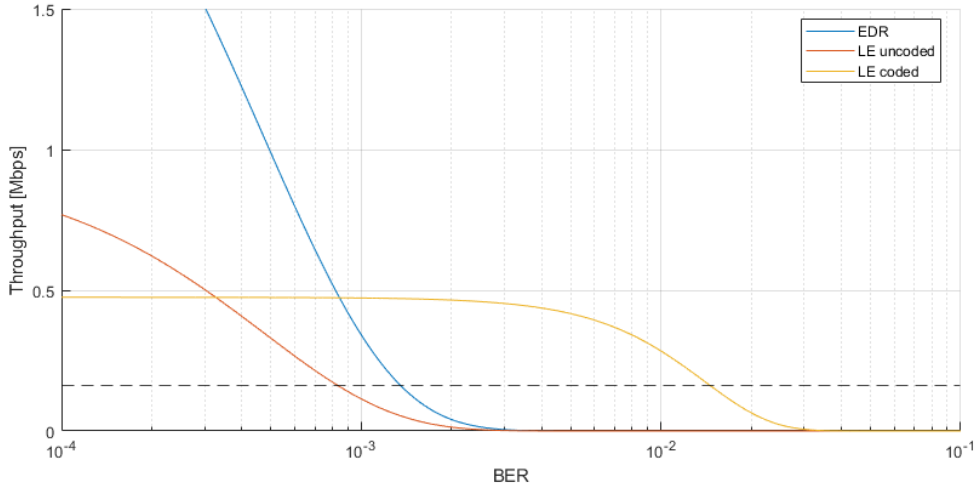

Figure 4.12: Throughput versus BER. Black dotted line represents minimum required throughput.

The empirical cumulative distribution function (cdf) of the BER for the EDR and LE modulation schemes, based on the 128 SNR samples from the simulations is given in figure 4.13. This figure shows the percentage of samples with a BER lower than a particular value. The CDF of the EDR modulation scheme is significantly lower than that of the LE variant due to the higher complexity of the 8DPSK scheme versus the GFSK. Therefore bit errors are more likely for this scheme. The colored points show the intersection with the CDF-line for with the maximum allowed BER, which was found in figure 4.12. The points give us the percentage of samples in which the minimum bitrate can be achieved. The failure rate, which gives the time that the bitrate cannot be achieved is given in table 4.7

Bluetooth Type	**Failure Rate**
EDR	58.6%
LE uncoded	15.6%
LE coded (S=2)	7.8%

Table 4.6: Intersection Values .

The failure rates are derived from 128 samples. The exact failure rate can thus vary, but the simulations give an indication. These results can thus be used to for instance determine the best communication protocol, modulation scheme and type

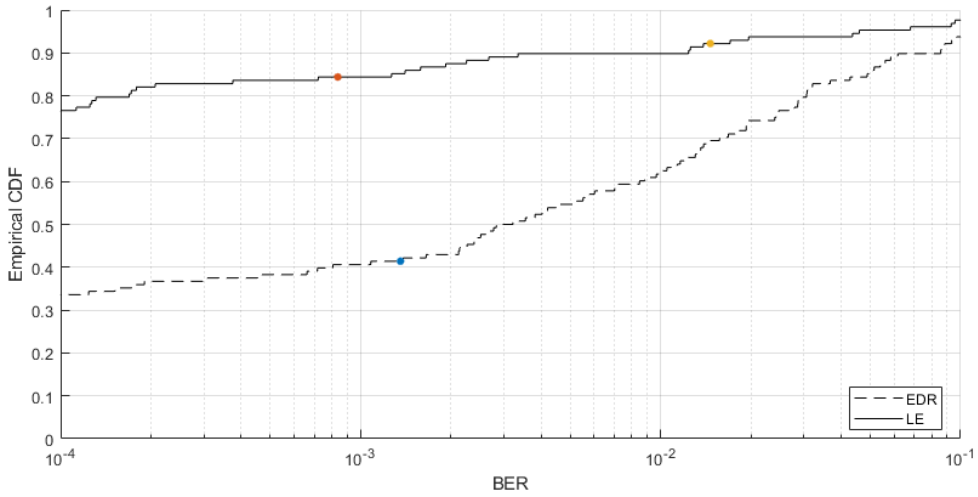

Figure 4.13: Empirical CDF of BER, with dotted lines representing the corresponding maximum allowed BER.

of physical layer are best suited for this scenario. Bluetooth EDR is able to achieves high data rate, but unreliable when the BER rises. Bluetooth LE performs much better due to its simpler modulation scheme. The FEC addition increases the reliability even more. The data rate is however limited. In this particular scenario in which a reliable 160 kbps connection is required, the Bluetooth LE with FEC performs best.

There are however some assumption made, which could reduce the achievable throughput and could cause the fail rate to increase. They are:

- The packet overhead: The packet does not only contain payload.
- Inter Frame Space (IFS): time between two successive packets.
- Connection interval: Limited number of packets that can be sent during one connection event.
- Time between two connection events.

LCR and ADF

The fail rate indicates when the minimal throughput cannot be achieved for all positions. In reality, a patient with a patient monitor will not experience a partial successful connection. When the patient moves or when the environment changes, a successful connection can suddenly fail or vice versa. This can be simulated by drawing an artificial path through the hospital rooms. A path is drawn wherein a patient walks around in every room and through the hallway at a speed of $5km/h$, the SNR changes according to figure 4.14. The SNR value of 11.495 dB is drawn as well. This level corresponds to the minimum SNR level to achieve the before

mentioned bitrate when the coded variant of Bluetooth LE is used.

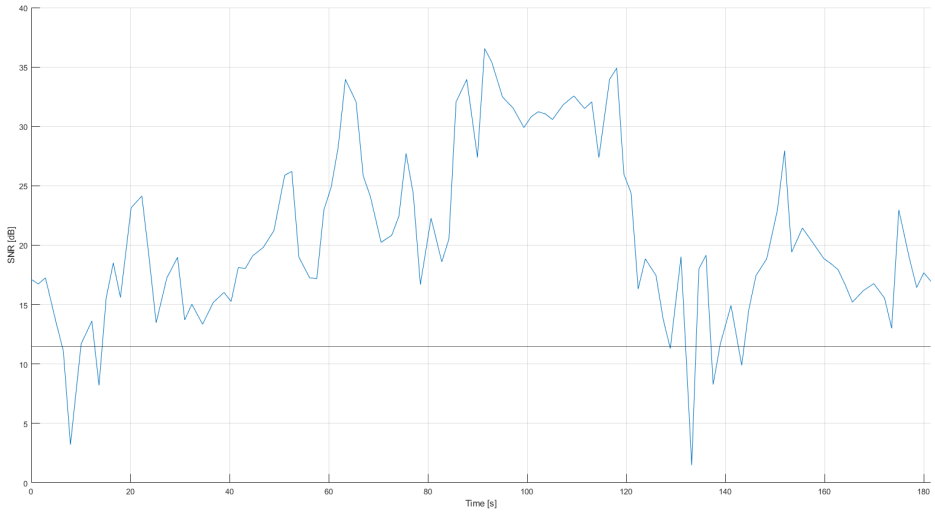

Figure 4.14: SNR when walking through hospital.

The SNR-level crosses the minimum required SNR six times (from below to above) yielding a LCR of 1.984 times per minute. The average duration of a fade is 1.997s. Short fades do however not necessarily lead to connection errors. Failed packet will simply be re-transmitted. The delay induced by them however, could potentially be critical in medical scenarios.

Level Crossing Rate	$0.033s^{-1}$
Average Duration of Fades	$1.997s$

Table 4.7: Intersection Values .

Chapter 5

Conclusions and Recommendations

5.1 Conclusions

The effect of simplifications in a RL simulator on the computational complexity and the accuracy of radio channel characteristics has been investigated. It has been found that the computational complexity of the simulation is mainly dependent on the simulator settings: the reflection order and ray density. Especially the latter, which causes an exponential increase in complexity when raised.
The accuracy of the RL simulator is mainly determined by the modeled environment and antennas. Simplifications on these aspects have a negligible effect on the computational complexity so a maximum modeling accuracy should be pursued. The accuracy of the environment likely depends on available (3D) floor plans and the required detailedness depends on the operating frequency, as is shown in the literature.
Executed simulations have shown that the used radiation pattern has a big impact on the radio channel characteristics. Using measured radiation patterns which do not contain phase information instead of parametric antennas reduced the average discrepancies in received power, mean delay and delay spread by 8dB, 18ns and 10ns respectively. These values correspond to a reduction in discrepancies of approximately 50%, 90% and 70% respectively. Including phase information will presumably further decrease the discrepancies.

If accurate environmental models and antenna patterns are used within RL simulations, wireless links can be evaluated in a end-use environment. Given a wireless technology and minimal required bitrate, the fail rate, level crossing rate and average duration of fades can be computed in a simulated end-use environment.
The main argument to use RL-simulators for this purpose is its ability to simulate many radio channels quickly with a decent accuracy. This argument does not hold for Ansys HFSS SBR+, as every radio channel is simulated independently.

5.2 Recommendations

The computational complexity of the RL-simulator is mainly determined by its simulator settings. A minimal reflection order of 3 is recommended. Lower values cause significantly large errors. The benefit of higher orders is limited, but so are the costs. The minimal value for the ray density is recommended to be 1. Ray densities below this value will not lead to any reduction in computational complexity. Higher value for the ray density are recommended if the available processing power and/or simulation time is available.

Although ANSYS SBR+ proved to be very capable of achieving accurate channel characteristics while keeping the complexity of the simulation low, it is not very well suited for radio propagation simulations since it solves every channel independently. It is therefore recommended to inform if steps within the SBR+ workflow can be reused for multiple channels in the near future, or to use an alternative RL-simulator.

Bibliography

[1] A. F. Molisch, *Wireless Communications*, 2nd ed. 2011 John Wiley & Sons Ltd., 2010.

[2] M. Gan, "Accurate and Low-complexity Ray Tracing Channel Modeling," no. November, 2015.

[3] V. Degli-esposti, F. Fuschini, E. M. Vitucci, and S. Member, "Scattering From Buildings," vol. 55, no. 1, pp. 143–153, 2007.

[4] J. B. Keller, "Geometrical theory of diffraction," *Journal of the Optical Society of America*, vol. 52, no. 2, pp. 116–130, 1962.

[5] R. Kouyoumjian and P. Pathak, "A uniform geometrical theory of diffraction for an edge in a perfectly conducting surface," *Proceedings of the IEEE*, vol. 62, no. 11, pp. 1448–1461, 1974.

[6] P. H. Pathak, W. D. Burnside, and R. J. Marhefka, "A Uniform GTD Analysis of the Diffraction of Electromagnetic Waves by a Smooth Convex Surface," *IEEE Transactions on Antennas and Propagation*, vol. 28, no. 5, pp. 631–642, 1980.

[7] F. Fuschini, E. M. Vitucci, M. Barbiroli, G. Falciasecca, and V. Degli-Esposti, "Ray tracing propagation modeling for future small-cell and indoor applications: A review of current techniques," *Radio Science*, vol. 50, no. 6, pp. 469–485, 2015.

[8] B. S. Lee, A. R. Nix, J. P. Mcgeehan, M. V. Building, and W. Road, "A Spatio-Temporal Ray Launching Propagation Model for UMTS Pic0 and Microcellular Environments," *IEEE VTS 53rd Vehicular Technology Conference, Spring 2001. Proceedings (Cat. No.01CH37202)*, 2001.

[9] M. Särestöniemi, M. Hämäläinen, and J. Iinatti, "An overview of the electromagnetic simulation-based channel modeling techniques for wireless body area network applications," *IEEE Access*, vol. 5, pp. 10 622–10 632, 2017.

[10] V. Degli-Esposti, G. Lombardi, C. Passerini, and G. Riva, “Wide-band measurement and ray-tracing simulation of the 1900-MHz indoor propagation channel: Comparison criteria and results,” *IEEE Transactions on Antennas and Propagation*, vol. 49, no. 7, pp. 1101–1110, 2001.

[11] M. Peter, W. Keusgen, and R. Felbecker, “Measurement and ray-tracing simulation of the 60 GHz indoor broadband channel: Model accuracy and parameterization,” *IET Seminar Digest*, vol. 2007, no. 11961, 2007.

[12] S. H. Han and S. K. Park, “Performance analysis of wireless body area network in indoor off-body communication,” *IEEE Transactions on Consumer Electronics*, vol. 57, no. 2, pp. 335–338, 2011.

[13] S. L. Cotton, A. McKernan, A. J. Ali, and W. G. Scanlon, “An experimental study on the impact of human body shadowing in off-body communications channels at 2.45 GHz,” *Proceedings of the 5th European Conference on Antennas and Propagation, EUCAP 2011*, pp. 3133–3137, 2011.

[14] T. Welch, R. L. Musselman, B. A. Emessiene, P. D. Gift, D. K. Choudhury, D. Cassadine, and S. Yano, “The Effects of the Human Body on UWB Signal Propagation in an Indoor Environment Thad.” *Journal of Electromagnetic Waves and Applications*, vol. 26, no. 4, pp. 560–569, 2012.

[15] M. Ghaddar, L. Talbi, T. A. Denidni, and A. Charbonneau, “Modeling human body effects for indoor radio channel using UTD,” *Canadian Conference on Electrical and Computer Engineering*, vol. 3, no. l, pp. 1357–1360, 2004.

[16] H. Yongming, A. Charbonneau, L. Talbi, and T. A. Denidni, “Effect of human body upon line-of-sight indoor radio propagation,” *Canadian Conference on Electrical and Computer Engineering*, no. May, pp. 1775–1778, 2006.

[17] E. Staudinger, J. Stephan, Y. Corre, and Y. Lostanlen, “Impact of human crowd activity on indoor wireless channels - Assessment and modeling,” *2013 10th Workshop on Positioning, Navigation and Communication, WPNC 2013 - Proceedings*, 2013.

[18] A. F. Molisch, K. Balakrishnan, D. Cassioli, C.-c. Chong, S. Emami, A. Fort, J. Karedal, J. Kunisch, H. Schantz, U. Schuster, and K. Siwiak, “IEEE 802.15.4a channel model,” pp. 1–40, 2005.

[19] A. Bamba, W. Joseph, J. B. Andersen, E. Tanghe, G. Vermeeren, D. Plets, J. Ø. Nielsen, and L. Martens, “Experimental assessment of specific absorption rate using room electromagnetics,” *IEEE Transactions on Electromagnetic Compatibility*, vol. 54, no. 4, pp. 747–757, 2012.

[20] M. Kim, Y. Konishi, S. Member, and Y. Chang, “Large Scale Parameters and Double-Directional Characterization of Indoor Wideband Radio Multipath Channels at 11 GHz,” vol. 62, no. 1, pp. 430–441, 2014.

[21] “ANSYS HFSS Technical Notes.”

[22] ITU-R - Radiocommunication Sector of ITU, “Recommendation ITU-R P.2040-1: Effects of building materials and structures on radiowave propagation above about 100 MHz,” *Recommendation ITU-R P.2040*, vol. 1, 2015. [Online]. Available: http://www.itu.int/rec/R-REC-P.2040-0-201309-I

[23] B. H. Fleury, “An Uncertainty Relation for WSS Processes and Its Application to WSSUS Systems,” vol. 44, no. 12, pp. 1632–1634, 1996.

[24] S. E. Johnston and P. D. Fiore, “Close-Range Outdoor Wireless Channel Sounding,” pp. 1919–1923, 2011.

[25] C. E. Shannon, *The Mathematical Theory of Communication*, 1997, vol. 14, no. 4.

[26] J. R. Luque, M. J. Morón, and E. Casilari, “Analytical and empirical evaluation of the impact of Gaussian noise on the modulations employed by Bluetooth Enhanced Data Rates,” pp. 1–11, 2012.

[27] M. Fischer, A. Adalan, and A. Scholtz, “Architecture of a Modular IEEE 802.15.4a Ultra-Wideband Transmitter,” *Microelectronics*, 2008.

[28] Decawave Ltd 2017, “DW1000 USER MANUAL.”

Appendix A

eHealth House

Figure A.1: Livingroom.

Figure A.2: Glasswall from Outside.

Figure A.3: Door towards Bedroom(left) and Person holding Node(right).

Figure A.4: Closet in Bedroom.

Figure A.5: Bed in Bedroom.

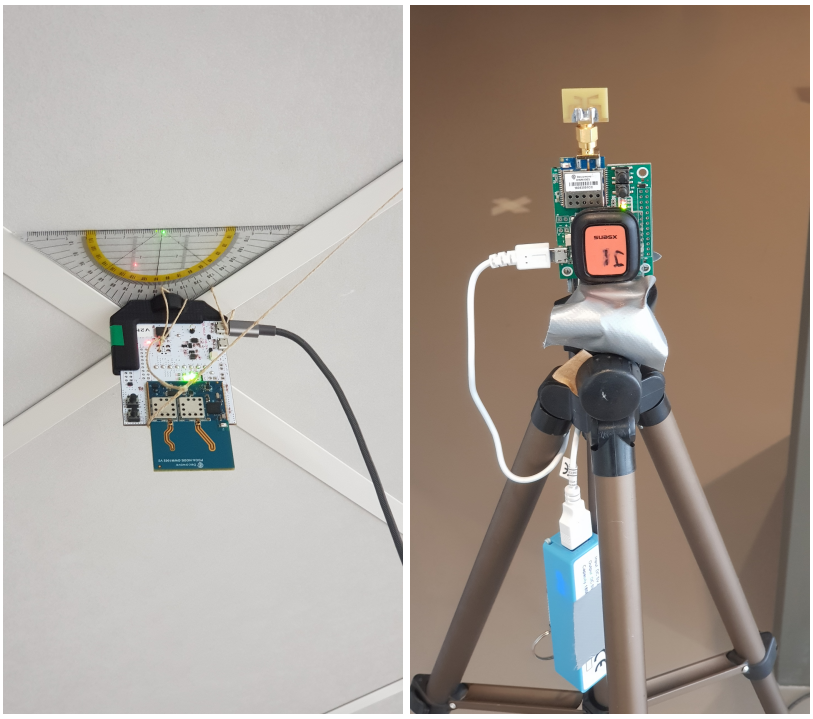

Figure A.6: Anchor Fixed to the Ceiling (left) and Node Mounted on a Tripod(right).

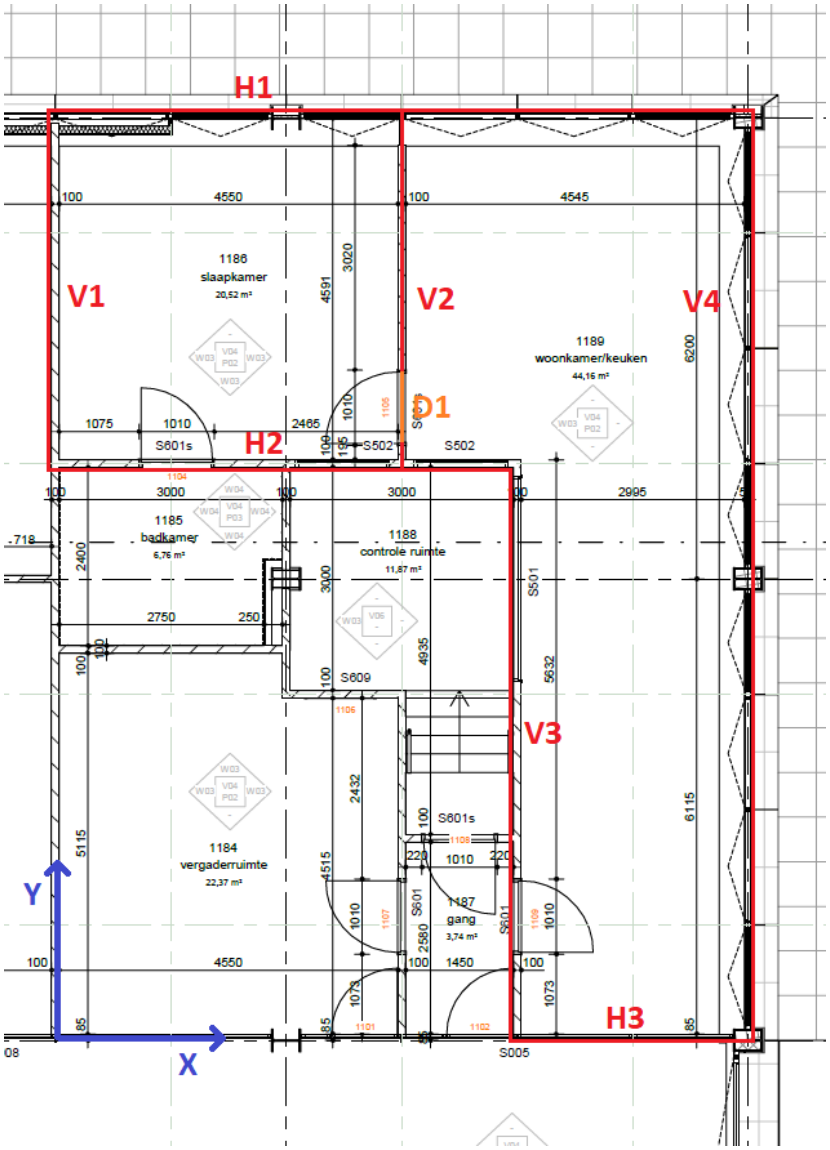

Figure A.7: Floorplan with labeled wall and coordinate system.

Label	x_{left} [mm]	x_{right} [mm]	y_{bottom} [mm]	y_{top} [mm]
H1	0	9380	12400	12485
H2	0	6300	7709	7809
H3	6200	9380	0	85
V1	0	100	7709	12485
V2	4650	4750	7809	12400
V3	6200	6300	0	7809
V4	9295	9380	0	12485
D1	4650	4750	8004	9014

Table A.1: eHealth House Wall Coordinates. H=horizontal walls, V=vertical walls, D=doorway.